THE TRANSFERRED HYPERFINE EFFECT IN $ErCl_3$

Thesis for the Degree of Ph. D.
MICHIGAN STATE UNIVERSITY
DENNIS E. GALLUS
1971

This is to certify that the

thesis entitled

THE TRANSFERRED HYPERFINE EFFECT IN $ErCl_3$

presented by

Dennis E. Gallus

has been accepted towards fulfillment
of the requirements for

Ph.D. degree in Physics

Major professor

Date 30 July, 1971

ABSTRACT

THE TRANSFERRED HYPERFINE EFFECT IN $ErCl_3$

by

Dennis E. Gallus

An experiment was performed to indirectly measure the transferred hyperfine effect in paramagnetic $ErCl_3$ at 1.18 K and 500 G applied field. Directions of the principal axes were determined and the applied field rotated through planes containing the principal axes. Data on transition frequencies vs. angle of applied field was taken, using a minipulser.

An effective field tensor was fitted to resonance data, and the transferred hyperfine interaction tensor decoupled from it, using measured susceptibility data and evaluating the dipole-dipole interaction by a computer summation over lattice sites.

The greatest contribution to the internal field by the transferred hyperfine effect occurred for a magnetic field applied in the mirror plane, near its intersection with the cleavage plane. The applied field was decreased by 70% due to the transferred hyperfine field.

The transferred hyperfine interaction tensor was decomposed into an isotropic part $A_s\underline{\underline{1}}$ and an anisotropic part $\underline{\underline{A}}_p$. The isotropic part is $A_s = 3.7 \times 10^{-4}\ cm^{-1}$. $\underline{\underline{A}}_p$ was analyzed in terms of σ and π-bond contributions, and $A_\sigma - A_\pi = -6. \times 10^{-4}\ cm^{-1}$ for both π orbitals. This indicates a greater interaction between the Cl^{35} nucleus and the holes in 3p electron orbitals perpendicular to the internuclear radius.

THE TRANSFERRED HYPERFINE EFFECT IN $ErCl_3$

By

Dennis E. Gallus

A THESIS

Submitted to
Michigan State University
in partial fulfillment of the requirements
for the degree of

DOCTOR OF PHILOSOPHY

Department of Physics
1971

To Prudence

ACKNOWLEDGMENTS

I express sincere thanks to Dr. E. H. Carlson, for both suggesting this project and providing a great amount of help and encouragement during the course of the work. I also thank Dr. J. P. Hessler for many useful conversations, and Mr. D. H. Current for help in data taking.

TABLE OF CONTENTS

LIST OF TABLES

LIST OF FIGURES

I INTRODUCTION

Nuclear magnetic resonance has proven to be a particularly useful tool for analyzing the degree of covalency of the metallic halides. This technique is especially applicable to a paramagnetic salt such as $ErCl_3$, in which the Cl^{35} nucleus undergoes both an electric quadrupole and a transferred hyperfine interaction, with a very strong resonance signal.

An asymmetric charge distribution around the Cl^{35} nucleus will produce an electric field gradient which will couple to the quadrupole moment of the nucleus. In forming a covalent bond, such as in $ErCl_3$, the Cl^- ion transfers some electronic charge to the Er^{3+} ion. This transfer of charge produces holes in the Cl^- 3s and 3p orbitals, giving rise to an electric field gradient and hence a quadrupole interaction. But since unequal amounts of spin-up and spin-down charge are transferred, a net spin density exists which interacts with the Cl^{35} nucleus via the transferred hyperfine interaction.

The transferred hyperfine interaction is not the only perturbation to the quadrupole interaction. In the presence of a magnetic field, there are Zeeman and dipole-dipole interactions as well. The purpose of this thesis is to account for all these interactions in a Hamiltonian, and to evaluate the transferred hyperfine interaction tensor. This tensor is then used to estimate the fractional spin density in the Cl^- 3s and 3p orbitals, giving an insight into bonding modes.

The method employed is to fit an effective field tensor to the resonance data, and to decouple from it the transferred hyperfine tensor. The fitting of the tensor to the data, and the evaluation of the various interactions, are accomplished with the aid of a computer. Results are discussed in terms of σ and π bonding between the Cl^- and Er^{3+} ions.

II. THEORETICAL

General Theory and Hamiltonian

All nuclei of spin ≥ 1 possess an electric quadrupole moment which can interact with the gradient of any electric field present at that nucleus. The Hamiltonian for this interaction is the Quadrupole Hamiltonian,

$$H_Q = \underline{\underline{Q}} \cdot \underline{\underline{\nabla E}} \qquad (1)$$

where $\underline{\underline{Q}}$ is the tensor defining the quadrupole charge distribution in the nucleus and $\underline{\underline{\nabla E}}$ is the gradient of the electric field. The quadrupole moment $\underline{\underline{Q}}$ is a measure of the ellipticity of charge distribution in the nucleus, and is defined as

$$eQ = \tfrac{1}{2}\int (3z^2 - r^2)\rho(\underline{r})d^3x \qquad (2)$$

where $\rho(\underline{r})$ is the charge density. Q is positive for an egg-shaped nucleus, and negative for a saucer-shaped nucleus.

Because the nucleus possesses a spin $\underline{I}$ and a net charge, it also possesses a magnetic moment, $\underline{\mu}_n$,

$$\underline{\mu}_n = \gamma \hbar \underline{I} \qquad (3)$$

where γ is the magnetogyric ratio of the nucleus (γ = 2624. radians $sec^{-1}G^{-1}$ for Cl^{35}). The allowable nuclear spin states are quantized, and the component m_I of the nuclear spin vector in any direction can take only one of a set of discrete values +I, (I-1), ...-I; for Cl^{35}, 3/2 ... -3/2.

If one applies a steady magnetic field H to the nucleus, there is an interaction between the applied field and the magnetic moment $\underline{\mu}_n$. The Hamiltonian for this interaction is

$$\mathcal{H}_z = -\underline{\mu}_n \cdot \underline{H}. \qquad (4)$$

For small fields, this magnetic interaction may be viewed as a perturbation of the quadrupole interaction, one that breaks up the two-fold degeneracy of the pure quadrupole frequency. See Appendix A for the diagonalization of the quadrupole Hamiltonian in the presence of a weak magnetic field.

There is also an interaction between the magnetic moments of the nucleus and the electrons of unfilled shells, or electrons in the unfilled shells of neighboring ions. The classical interaction energy E between two magnetic moments $\underline{\mu}_n$ and $\underline{\mu}_e$ is

$$E = \frac{\underline{\mu}_n \cdot \underline{\mu}_e - 3(\underline{\mu}_n \cdot \hat{r})(\underline{\mu}_e \cdot \hat{r})}{r^3} , \qquad (5)$$

where $\hat{r}$ is the unit vector from $\underline{\mu}_n$ to $\underline{\mu}_e$ and r is the distance between the two moments. If there is a distribution of electrons over many lattice sites, the total dipolar Hamiltonian is the sum over all the electron magnetic moments. The crystal is paramagnetic, the Er^{3+} magnetic moments are lined up with the applied field, and the electron magnetic moment must be replaced by its thermal average $\langle\mu_e\rangle$. Thus

$$\mathcal{H}_{dd} = \underline{\mu}_n \cdot \sum_j \frac{1 - 3\,\hat{r}_j \cdot \hat{r}_j}{r_j^3} \langle\mu_e\rangle \qquad (6)$$

where $\underline{r}_j$ is the vector from the nuclear magnetic moment to the j<u>th</u> electron.

Representing the sum by a symmetric, second rank interaction tensor $\underline{\underline{D}}$, and substituting the definitions

$$\underline{\mu}_n = \gamma\hbar\underline{I} \tag{7}$$

$$<\underline{\mu}_e> = -\mu_B \cdot \underline{\underline{g}} \cdot <\underline{S}> \tag{8}$$

where μ_B is the Bohr magneton, $\underline{\underline{g}}$ is the electron g-tensor[1], and $\underline{S}$ is the electron spin, one has

$$H_{dd} = -\gamma\hbar\mu_B\, \underline{I}\cdot\underline{\underline{D}}\cdot\underline{\underline{g}}\cdot<\underline{S}> \;. \tag{9}$$

According to the usual meaning of the term "hyperfine", that is, having extra-nuclear origin and coupling to the nuclear spin, the dipole-dipole interaction is a hyperfine term. In this work, however, the term "hyperfine" will refer only to the transferred hyperfine interaction between the Cl^{35} nucleus and the charge transferred in forming the Er-Cl bond, exclusive of the dipole-dipole coupling.

The Hamiltonian for the hyperfine interaction is

$$H_h = \underline{I}\cdot\underline{\underline{A}}\cdot\underline{S} \;. \tag{10}$$

$\underline{\underline{A}}$ is the second rank hyperfine interaction tensor. As will be shown later, it is the sum of an isotropic and an anisotropic part.

The dipole-dipole and hyperfine Hamiltonians written above are not very useful, because the spin $\underline{S}$ is not a clearly defined quantity. In a paramagnetic crystal, the electron magnetic moments align with the field, but thermal disorder resists this alignment. Due to the crystal structure, the magnetic moments are more easily aligned in certain directions than in others; the anisotropic electron g-tensor describes this. Further, there are spin relaxation effects.[2] What all of this implies is that the nucleus responds only to an average electronic field, proportional to the spin average $<\underline{S}>$. Thus, the hyperfine Hamiltonian is better written

$$\mathcal{H}_h = \underline{I}\cdot\underline{\underline{A}}\cdot<\underline{S}>. \tag{11}$$

For a paramagnetic crystal, the magnetization $\underline{M}$ is proportional to the thermal-averaged spin:

$$\underline{M} = N\mu_B\underline{\underline{g}}\cdot<\underline{S}> \; ; \tag{12}$$

here, N is avogadro's number. Also,

$$\underline{M} = \underline{\underline{\chi}}\cdot\underline{H} \; . \tag{13}$$

Thus,

$$<\underline{S}> = \frac{\underline{\underline{g}}^{-1}\cdot\underline{\underline{\chi}}\cdot\underline{H}}{\mu_B N} \tag{14}$$

This defines the thermal-averaged spin in terms of measurable quantities.

The hyperfine tensor $\underline{\underline{A}}$ can be determined, at least phenomenologically, from plots of Cl^{35} transition frequencies. The various interactions are viewed as if they modified the applied magnetic field and produced an internal field which caused the splitting of the observed transition frequencies.

Writing the total Hamiltonian as

$$\mathcal{H} = \mathcal{H}_Q - \gamma\hbar\underline{I}\cdot\underline{H} - \gamma\hbar\mu_B\underline{I}\cdot\underline{\underline{D}}\cdot\underline{\underline{g}}\cdot<\underline{S}> + \underline{I}\cdot\underline{\underline{A}}\cdot<\underline{S}> \; , \tag{15}$$

$$= \mathcal{H}_Q - \gamma\hbar\underline{I}\cdot\left[\underline{\underline{1}} + \left(\underline{\underline{D}} - \frac{\underline{\underline{A}}\cdot\underline{\underline{g}}^{-1}}{\gamma\hbar\mu_B}\right)\cdot\frac{\underline{\underline{\chi}}}{N}\right]\cdot\underline{H} \; , \tag{16}$$

one has

$$\mathcal{H} = \mathcal{H}_Q - \gamma\hbar \underline{I}\cdot\underline{\underline{T}}\cdot\underline{H}, \tag{17}$$

with

$$\underline{\underline{T}} = \underline{\underline{1}} + [\underline{\underline{D}} - \frac{\underline{\underline{A}}\cdot\underline{\underline{g}}^{-1}}{\gamma\hbar\mu_B}]\cdot\frac{\underline{\underline{\chi}}}{N} . \tag{18}$$

The choice of signs is consistent with that of Shulman and Sugano[3] in the case of $KMnF_3$, which does not, however, have a quadrupole interaction.

For purposes of analysis, the total Hamiltonian is best separated into a quadrupole part and a magnetic part;

$$\mathcal{H} = \mathcal{H}_Q + \mathcal{H}_m . \tag{19}$$

The magnetic part of the Hamiltonian can be thought of as the interaction of the Cl^{35} nuclear spin with an effective internal magnetic field $\underline{H}_{eff}$:

$$\mathcal{H}_m = -\gamma\hbar\underline{I}\cdot\underline{H}_{eff} . \tag{20}$$

$\underline{H}_{eff}$ is the sum of the applied field and the internal fields due to the spin of the electron:

$$\underline{H}_{eff} = \underline{H} + \underline{H}_{dd} + \underline{H}_h \tag{21}$$

$$= \underline{\underline{T}}\cdot\underline{H} . \tag{22}$$

This equation defines the effective field tensor $\underline{\underline{T}}$, whose effect is to modify the applied field in such a way as to cause the Cl^{35} transition frequencies observed in the lab.

Theory Particular to $ErCl_3$

Now that the Hamiltonian for Cl^{35} in $ErCl_3$ has been written, the various terms must be evaluated in order to uncouple the transferred hyperfine interaction tensor. Solving equation (18) for $\underline{\underline{A}}$,

$$\underline{\underline{A}} = \gamma\hbar\mu_B(\underline{\underline{D}} - N(\underline{\underline{T}}-\underline{\underline{1}})\cdot\underline{\underline{\chi}}^{-1})\cdot\underline{\underline{g}} \quad . \tag{23}$$

The dipole-dipole term is evaluated by summing over the Er^{3+} lattice sites, using a computer program based on equation (6). $\underline{\underline{T}}$ is fitted from the data of transition frequencies vs. angle of applied field. The values of $\underline{\underline{\chi}}^{-1}$ and $\underline{\underline{g}}$ have been determined experimentally by Fairall, et al.[4]

The $\underline{\underline{A}}$ tensor obtained in this decoupling describes the total transferred hyperfine interaction between a Cl^{35} nucleus and its two nearest neighbor Er^{3+} ions. By means of similarity transformations and symmetry properties, one may separate out the effect of only one Er-Cl bond. Thus, one obtains $\underline{\underline{A}}_{Er}$, the transferred hyperfine interaction tensor in the Er system of axes, centered on the Cl^{35} ion, whose x' axis coincides with the Er-Cl internuclear radius. $\underline{\underline{A}}_{Er}$ may be decomposed into an isotropic component,

$$\underline{\underline{A}}_s = A_s\underline{\underline{1}} \tag{24}$$

and an anisotropic, traceless component $\underline{\underline{A}}_p$:

$$\underline{\underline{A}} = A_s\underline{\underline{1}} + \underline{\underline{A}}_p . \tag{25}$$

The separation of $\underline{\underline{A}}$ into isotropic and anisotropic parts is useful because it can then be used to deduce whether the Cl^- electron wave function has primarily s or p-state character. In forming the covalent bond, the charge transfer from the Cl^- to the Er^{3+} creates 3s and 3p holes in the Cl^- electron

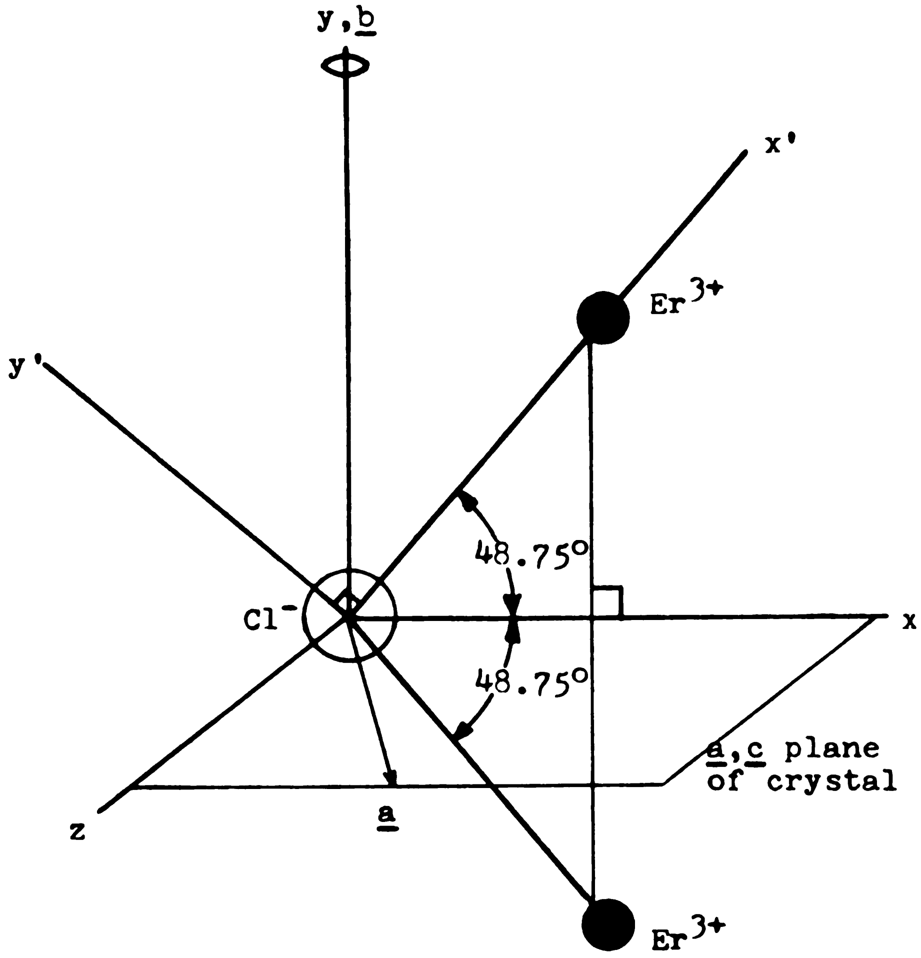

a, b are crystal lattice vectors

xz plane is mirror plane

(x,y,z) are principal axes

(x',y',z') are Er system of axes

Figure 1: Principal axes and Er axes

distribution. The total Cl^- electron wave function is thus a sum of s and p-state wave functions. A_s describes a hyperfine interaction between the Cl^{35} nucleus and the net spin in the 3s holes; $\underline{\underline{A}}_p$ describes an interaction between the nucleus and the 3p(x'), 3p(y'), and 3p(z') orbital holes.

The diagonal elements of $\underline{\underline{A}}_{Er}$ are

$$A_{ii} = A_s + \sum_{j=x',y',z'} A_{p(j)}(3\cos^2\theta_{ij} - 1). \qquad (26)$$

$\underline{\underline{A}}_p$ being traceless, it has only two principal elements.[5] Hence, one cannot determine the individual contributions of the three 3p orbitals. But one can deduce the isotropic term and the pairwise differences between the three p-dipolar hyperfine interactions $A_{3p(i)}$. Writing equation (26) in explicit form, $\cos^2\theta_{ij} = 0$, $\cos^2\theta_{ii} = 1$, and

$$A_{x'x'} = A_s + 2A_{3p(x')} - A_{3p(y')} - A_{3p(z')} \qquad (27)$$

$$A_{y'y'} = A_s - A_{3p(x')} + 2A_{3p(y')} - A_{3p(z')} \qquad (28)$$

$$A_{z'z'} = A_s - A_{3p(x')} - A_{3p(y')} + 2A_{3p(z')}. \qquad (29)$$

Adding these three equations, one sees

$$A_s = \frac{1}{3} \sum_{j=x',y',z'} A_{jj} . \qquad (30)$$

Subtracting equation (28) from equation (27), one sees

$$A_{x'x'} - A_{y'y'} = 3(A_{3p(x')} - A_{3p(y')}) \qquad (31)$$

hence

$$A_{3p(x')} - A_{3p(y')} = \frac{1}{3}(A_{x'x'} - A_{y'y'}) . \qquad (32)$$

Subtracting equation (29) from equation (27),

$$A_{x'x'} - A_{z'z'} = 3(A_{3p(x')} - A_{3p(z')}), \qquad (33)$$

$$A_{3p(x')} - A_{3p(z')} = \frac{1}{3} (A_{x'x'} - A_{z'z'}) \; . \tag{34}$$

Subtracting equation (29) from equation (28),

$$A_{y'y'} - A_{z'z'} = 3(A_{3p(y')} - A_{3p(z')}) \tag{35}$$

$$A_{3p(y')} - A_{3p(z')} = \frac{1}{3} (A_{y'y'} - A_{z'z'}) . \tag{36}$$

The 3p(x') orbital is along the internuclear radius, the line of bonding, while the 3p(y') and 3p(z') orbitals are perpendicular to the internuclear radius. In the notation of chemical bonding, 3p(x') would be designated a σ orbital, and 3p(y') and 3p(z') are designated π orbitals, π_y and π_z respectively. Symmetry does not, in the case of $ErCl_3$ crystal structure, allow one to say that π_y and π_z are equal. But one can determine relative amounts of the σ, π_y and π_z orbitals. From equation (32), using σ and π notation,

$$A_\sigma - A_{\pi_y} = \frac{1}{3} (A_{x'x'} - A_{y'y'}) \; . \tag{37}$$

From equation (34),

$$A_\sigma - A_{\pi_z} = \frac{1}{3} (A_{x'x'} - A_{z'z'}) . \tag{38}$$

And from equation (36),

$$A_{\pi_y} - A_{\pi_z} = \frac{1}{3} (A_{y'y'} - A_{z'z'}) . \tag{39}$$

The σ and π notation denotes the type of chemical bonding (or antibonding). The 3p-σ electrons are those in the σ bond, having no angular momentum about the internuclear radius. The 3p-π electrons are in π bonds, which do have angular momentum about this axis. Thus, A_σ interactions arise from an electron wave function in the Cl 3p orbitals which lie along the Er-Cl internuclear axis, and A_π interactions arise from an electron wave function in the Cl 3p orbitals perpendicular to this direction.

To appreciate the physical significance of the constants, consider the $^2P_{3/2}$ ground state of the Cl atom. The only contributions to the transferred hyperfine effect come from the single unpaired electron. Quantizing along the x axis, the asymmetry parameter $\eta = 0$, and $A_y = A_z$, and experimentally[6]

$$A_{3p(x')} = 51.2 \times 10^{-4}\ \text{cm}^{-1}. \qquad (40)$$

The isotropic hyperfine interaction constant for the Cl^- ion has been calculated to be

$$A_{3s} = 0.148\ \text{cm}^{-1}\ . \qquad (41)$$

These numbers are presented only to give an indication of the order-of-magnitude of the hyperfine interaction tensor.

III CRYSTAL STRUCTURE

$ErCl_3$ has a crystal structure isomorphic to $AlCl_3$, having a tetramolecular cell of the monoclinic space group C2/m. The ions occupy the following positions of point symmetry:[7,8]

4Er:(g), 2, $\pm(0u0;\frac{1}{2},u+\frac{1}{2},0)$

4Cl(1):(i),m, $\pm(u0v;u+\frac{1}{2},\frac{1}{2},v)$

8Cl(2):(j),1, $\pm(xyz;x\bar{y}z;x+\frac{1}{2},y+\frac{1}{2},z;x+\frac{1}{2},\frac{1}{2}-y,z)$

The parameters have not been determined for $ErCl_3$. They are taken as being the same as in YCl_3:

u(Y) = 0.166 u(Cl,1) = 0.211 v(Cl,1) = 0.247

x(Cl,2) = 0.229 y(Cl,2) = 0.179 z(Cl,2) = -0.240

The cell dimensions for $ErCl_3$ are (Å)

$a_0 = 6.80$ $b_0 = 11.79$ $c_0 = 6.39$ $\beta = 110°42'$

The crystal structure is a cubic close-packing of Cl^- ions distorted by the inclusion of Er^{3+} ions in one-third of the octahedral spaces. The ions are arranged in parallel layers as Cl-Er-Cl:Cl-Er-Cl:, with easy cleavage parallel to the plane of the layers; see Figure 2. This structure suggests an approximate three-fold axis perpendicular to the plane of the layers.

Carlson and Adams[7] have measured the nuclear quadrupole resonance parameters in $ErCl_3$, using the low field "elliptical cone"[9,10] method. For the four-fold Cl(1) site, they find $q = \pm 3.103\ \mathring{A}^{-3}$, and the x principal axis of this site is within 3° of the Er-Cl(1)-Er angle bisector. The two bisectors of the eight-fold Cl(2) sites are within 4° of the x principal axes of the Cl(2) sites. The remainder of the Carlson and Adams results are summarized in Table 1, where the asymmetry parameters η_{NQR} and bond angle θ_{NQR} are calculated from resonance data. The f_Q are the observed pure chlorine quadrupole resonance frequencies. Orientation of the principal axes of the crystal with respect to the lab axes can be seen from Figure 3.

TABLE 1

Summary of Carlson and Adams Results

	f_Q(kHz)	η_{NQR}	η_{calc}	θ_{NQR}
Cl(1) four-fold	4515.7±0.2	0.52±0.03	0.523	100.0°±0.6°
Cl(2) eight-fold	4456.6±0.2	0.53±0.02		100.2°±0.4°

Cl^- ions lying in the mirror plane are designated as four-fold sites; the eight-fold site Cl^- ions are situated between the mirror planes. This difference in location creates a difference in the electric field gradient at the respective sites. Hence the pure quadrupole frequency for the four-fold site differs from that of the eight-fold site.

As can be seen from a crystal diagram such as Figure 2, an approximate three-fold axis of symmetry exists in the crystal. Apart from the fact that they occupy different

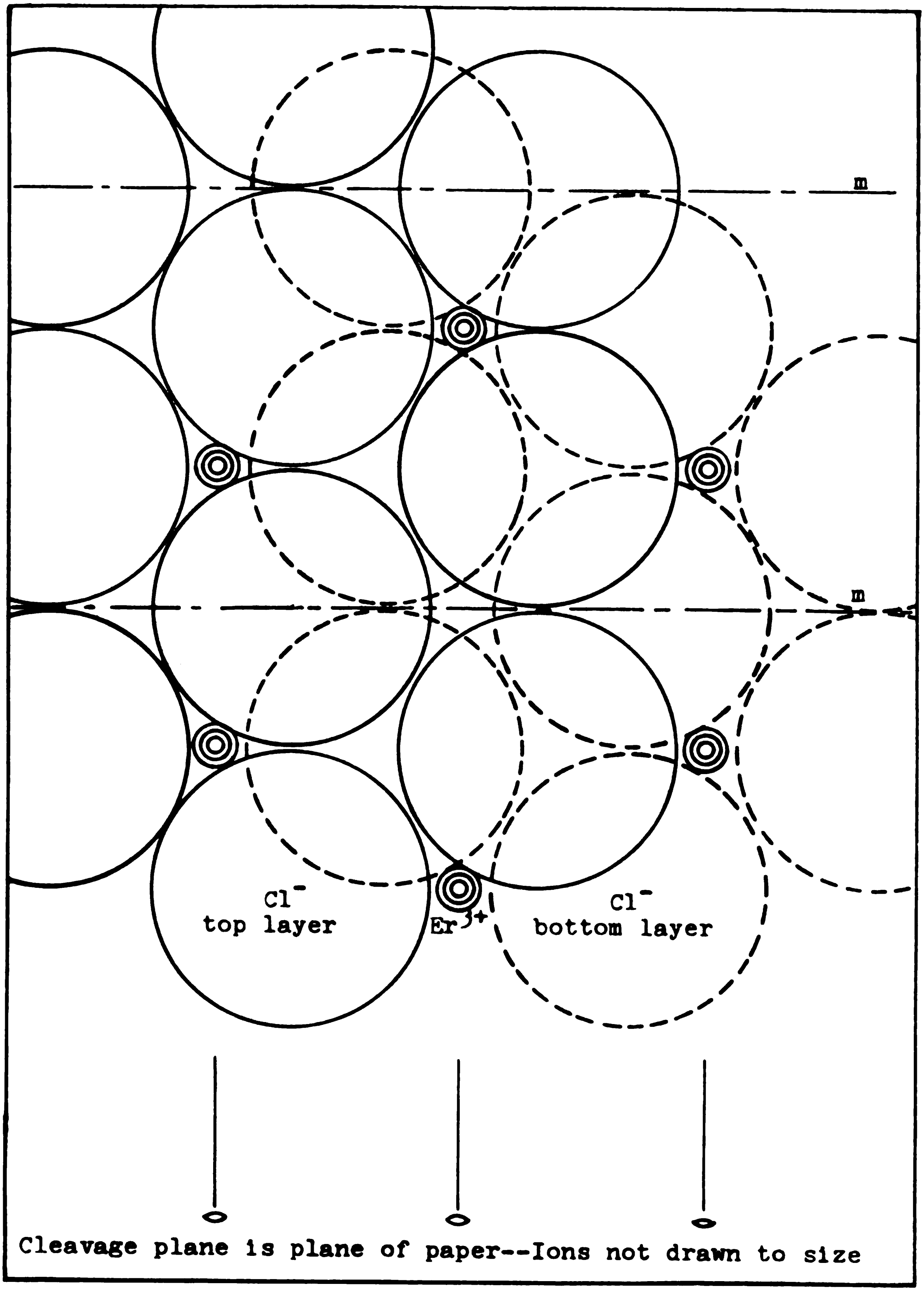

Figure 2: $ErCl_3$ Crystal Structure

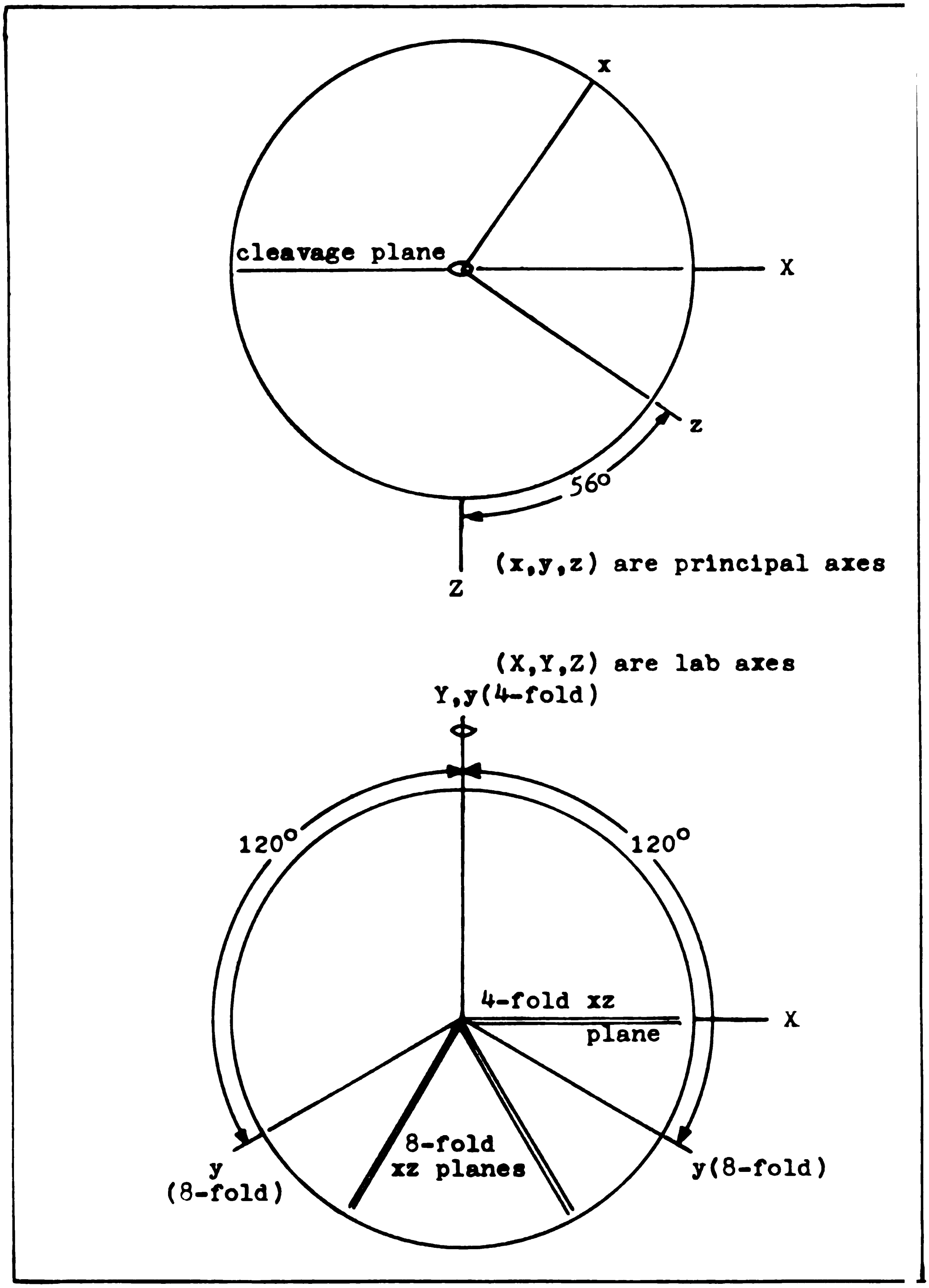

Figure 3: Relation between principal axes and lab axes

crystal sites, the Cl^- ions about this three-fold axis appear to be similarly situated with respect to Er^{3+} ions. This suggests that the tensor $\underline{\underline{T}}$ describing the effective field may also have three-fold symmetry, and this will be investigated in Appendix C.

This symmetry about the axis perpendicular to the cleavage plane is only approximate because the two sites have different quadrupole frequencies. The magnetic (Zeeman) splitting of the Cl^{35} transition frequencies appears to be three-fold symmetric about this axis, however.

IV SAMPLE PREPARATION

Single crystals of $ErCl_3$ are prepared from commercial anhydrous $ErCl_3$ powder. The powder, in a Vycor tube, is first dried by slow heating under vacuum in a vertical furnace. When waters of hydration are removed, the heat of the furnace is increased to melt the sample.

The fused, but impure, sample is then placed in the open end of a Vycor distillation tube and the tube sealed. The sealed tube is placed in a horizontal furnace whose right and left sides are controlled by separate variacs. During the entire distillation operation, the tube is under a vacuum of 10^{-6} mm Hg.

First the collecting side of the tube is heated to about 1000 C to outgas impurities from the tube. This side is then cooled to a temperature just slightly higher than the melting point of $ErCl_3$. Now the sample end of the tube is heated above the melting point, until the $ErCl_3$ gradually vaporizes and distills across to the collecting side of the tube, leaving behind involatile impurities. Violent boiling of the sample must be avoided, or splashing, hence contamination, will result. The pure $ErCl_3$ condenses on the walls of the collecting side of the tube, then runs down the walls into the ampule. See Figure 4.

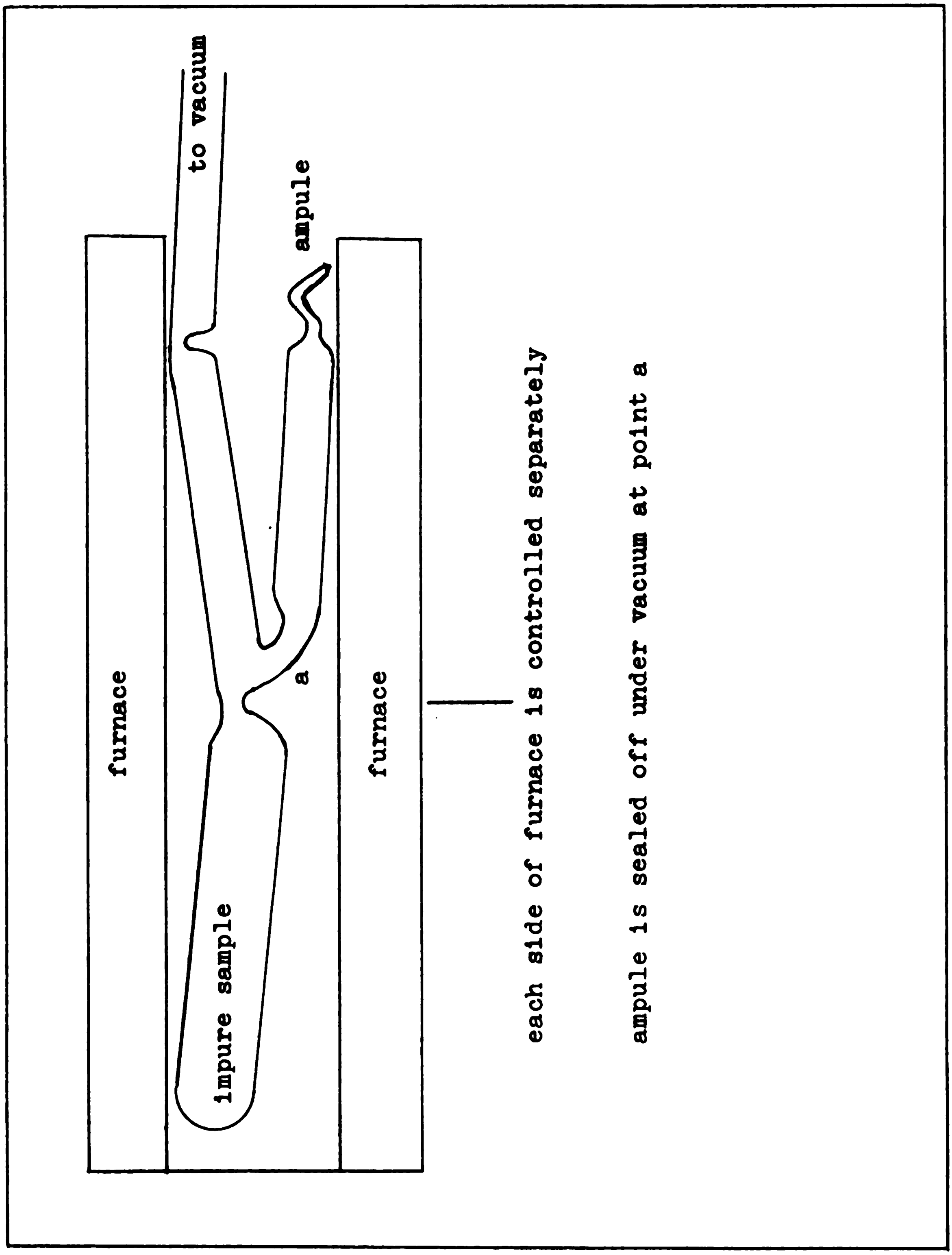

each side of furnace is controlled separately

ampule is sealed off under vacuum at point a

Figure 4: Distillation tube in furnace

When most of the $ErCl_3$ is distilled across, the distillation tube is cooled and the ampule sealed off under vacuum. A single crystal is grown in the ampule by lowering it through a gradient furnace. Before lowering is begun, the position of the ampule is repeatedly adjusted until several crystals form in the s-shaped tail of the ampule. The sample is then molten and at a temperature only slightly above the melting point; only the tip of the tail extends from the heated zone of the furnace. The crystals which form in the tail are examined at twelve hour intervals, and the actual dropping of the ampule through the furnace not begun until a crystal is present in the tail with its cleavage plane oriented in a favorable direction. The ampule is then lowered for approximately six days, and cooled slowly.

The ampule is sawed open with a diamond saw, and the crystal immersed in mineral oil. In order to prepare a spherical sample, a single crystal with no cleaving evident along its length is needed. The crystal is hand-ground with a slowly revolving grinding wheel, being continually bathed in mineral oil. Roundness is determined crudely by passing the crystal sample through holes drilled in a sheet metal strip. Only an approximately spherical shape is attainable by this method, and care must be taken to get that, as the crystal cleaves very easily when oil-soaked.

V SAMPLE MOUNTING AND LAB COORDINATES

For an experiment, the sample is placed in a rotatable goniometer attached to a cryostat. The goniometer can be rotated through more than 360° about its horizontal axis; this axis is taken as the lab Z direction. The lab Y axis is taken to be pointing up; lab X is then horizontal and perpendicular to Y and Z, so a right-handed system results. When the crystal is mounted on the goniometer, the cleavage plane is perpendicular to the plane of rotation of the goniometer. Hence, X and Y lie in the cleavage plane of the crystal.

The lab angle ϕ_{lab} is read off of the face of the goniometer by pointing a flashlight through the unsilvered portion of the dewar. The goniometer is marked in divisions of 5°, with a major division every 30°. Accuracy of aligning the goniometer is estimated at ±1°.

The magnet, rotating about the Y axis, defines θ_{lab}; an aluminum scale running about the base of the magnet is marked at intervals of 1°. The magnet pointer indicates 0° with the field along Z. When setting up each run, care is taken so that the magnet pointer reads 270° when the magnet pole faces are parallel to the Z direction.

The goniometer consists of a flat nylon disc centered on a brass bearing. The disc may be rotated from outside the dewar by means of a rotatable rod which moves a wire and pulley. Depending upon the shape of the crystal sample, it is mounted either directly on the goniometer, or held in a detachable nylon cup. Samples shaped like sections of cylinders are mounted directly on the goniometer disc, being held in place with vacuum grease and a small nylon clamp, which is screwed down with nylon screws. By pressing the cleavage plane of the crystal directly onto the plane of the disc, one insures that the cleavage plane is perpendicular to the axis of rotation of the goniometer.

Spherical samples are placed in the nylon cup and held in place with soft clay. In the case of cylindrical samples, a coil of #28 varnished wire could be wound directly on the sample. In the case of spherical samples, the coil must be wound around a thin paper cylinder whose radius is slightly larger than the radius of the sphere. This coil is then inserted in the nylon cup and held in place with clay. Coil leads are made long enough to avoid binding when the goniometer is rotated. During a long experiment, care must be taken to avoid rotating the goniometer in only one direction, to avoid the problem of snarled leads.

Before placing the spherical sample in the cup, a small part is cut off in the direction of cleavage to leave a flat spot. This spot is mounted facing out of the cup, and a small, flat mirror fragment is affixed to the flat spot with grease. Thus the mirror is parallel to the cleavage plane. The goniometer is then rotated, and the reflection of a target located above the plane of the disc is observed.

Position of the sphere is adjusted until the goniometer can be rotated without causing the image of the target as seen in the mirror to move. The cleavage plane of the crystal is then perpendicular to the axis of rotation of the goniometer disc.

When the cryostat is inserted in the dewar, the plane of rotation of the goniometer must be parallel to the field direction when the magnet pointer is set at 270°. To this end, a laser beam is reflected from a small mirror, mounted parallel to the cleavage plane of the crystal, and the rod supporting the goniometer turned. When the reflections from this mirror and a mirror perpendicular to the pole faces of the magnet coincide with the laser source (the laser being situated about ten feet away), the apparatus is in good adjustment, and a cartesian system established.

VI EXPERIMENTAL PROCEDURE

Locating the Principal Axes

All frequencies referred to are Cl^{35} transition frequencies. The signals of Cl^{37}, in addition to being only 25% as strong, are lower in frequency by a factor of $Q^{37}/Q^{35} = 0.785$; Q is the nuclear quadrupole moment. The Cl^{37} frequencies were not sought.

Carlson and Adams[7] give the orientation of the x and z principal axes with respect to the cleavage plane. But the orientation of the y axis in the cleavage plane must be determined every time a crystal is mounted on the goniometer. Thus, the first thing done in each experiment was to determine the location of the principal axes of the crystal.

At 77 K, observing free induction decay on an oscilloscope and using a minipulser[11], the four-fold site pure quadrupole frequency was traced by rotating the magnet through θ_{lab} to find the signal for every 5° change in position of the goniometer. The applied field was 500 G. Refer to Data Table 11 in Appendix D. These loci of zero-splitting were plotted on a stereographic net, and the resulting closed figure rotated up to become an ellipse centered on the pole. Using the "elliptical cone" method[9] for the low field case, the orientations of the principal axes were determined.

The orientation of the x and z principal axes with respect to the cleavage plane was found to agree with that of Carlson and Adams. See Figure 3.

General Experimental Procedure

An applied magnetic field of 500 G was rotated through the cleavage plane at a temperature of 1.18 K. Transition frequencies are plotted in Figure 5 and the data is listed in Data Table 12 in Appendix D. From the graph, it was concluded that an error of 10° in the assigned direction of the y principal axis had occurred previously in rotating up the ellipse. It was found that the orientation of the y principal axis could be located much more precisely and easily by sweeping the frequency while rotating the magnetic field through the cleavage plane of the crystal. The determination of the direction of the y axis by this method should be accurate to within one or two degrees.

Succeeding runs followed the same format: after aligning the apparatus, the crystal was cooled to 1.18 K. The applied field was first rotated through the cleavage plane to determine the locations of the y principal axes of the four-fold and eight-fold sites. Orientations of the x and z principal axes were then taken to be as in Figure 3. Knowing the locations of the y principal axes, the goniometer could be set so that the plane of rotation of the magnet included one or two principal axes of either the four-fold or eight-fold site. Representative data and figures are summarized in Table 2. An interpretation of the various figures follows.

TABLE 2

Summary of Data

Figure	Data Table*	Plane of Rotation of H
5	12	Cleavage
6	13	xz of four-fold
7	14	⊥ cleavage, containing y of four-fold
8	15	xz of eight-fold

*In Appendix D

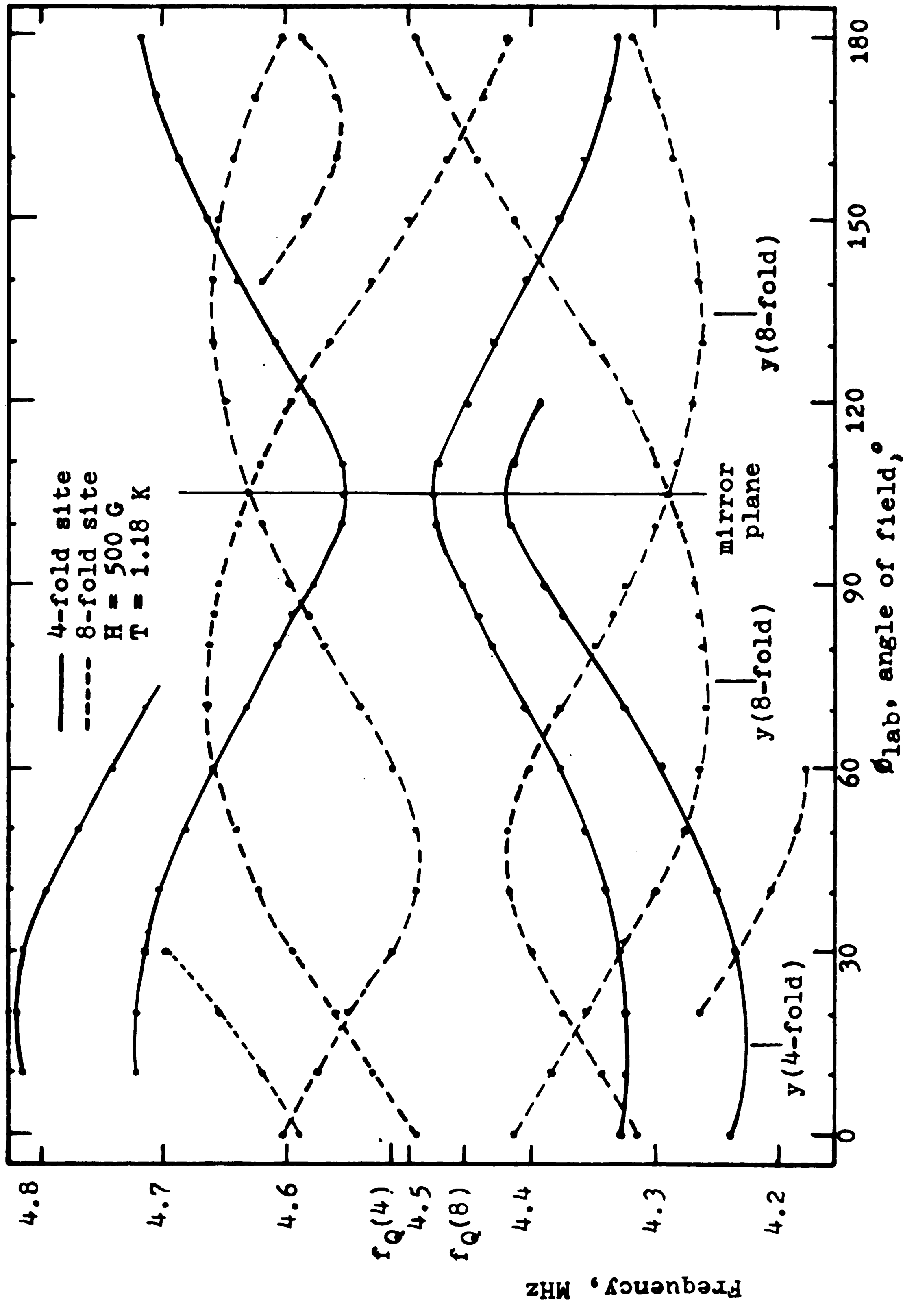

Figure 5: H in cleavage plane

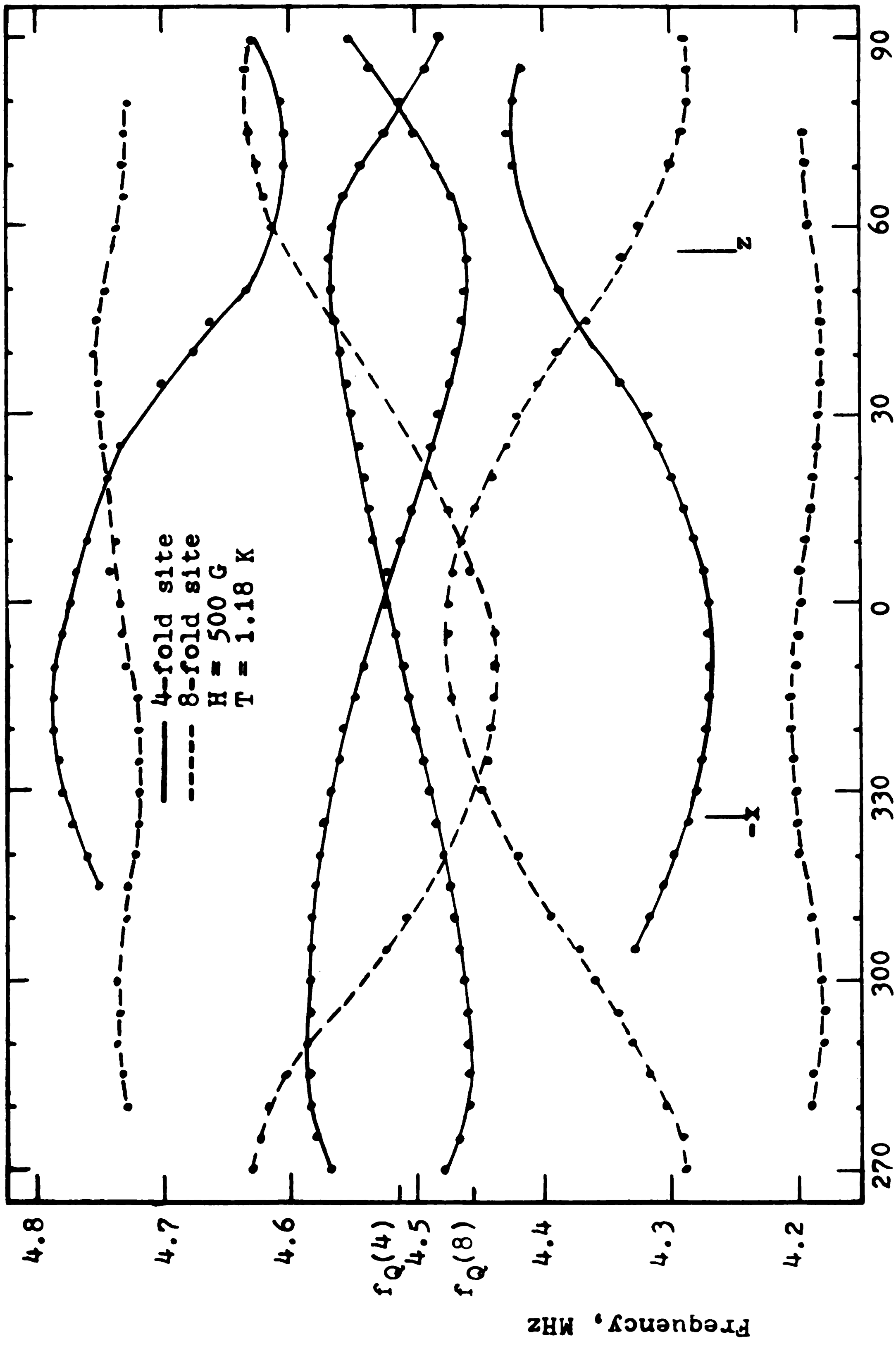

Figure 6: H in xz principal axis plane, 4-fold site

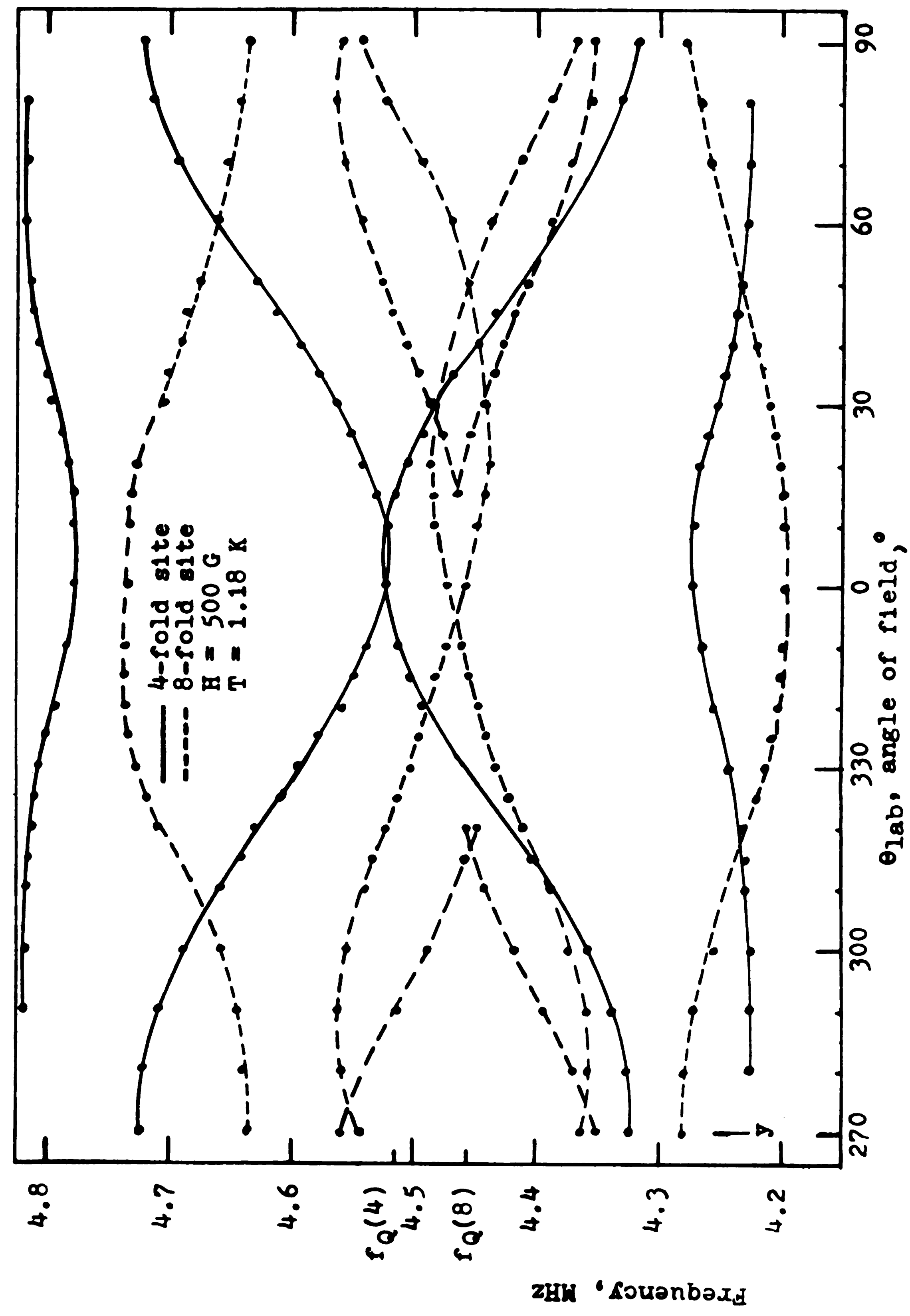

Figure 7: H in plane ⊥ cleavage containing y, 4-fold site

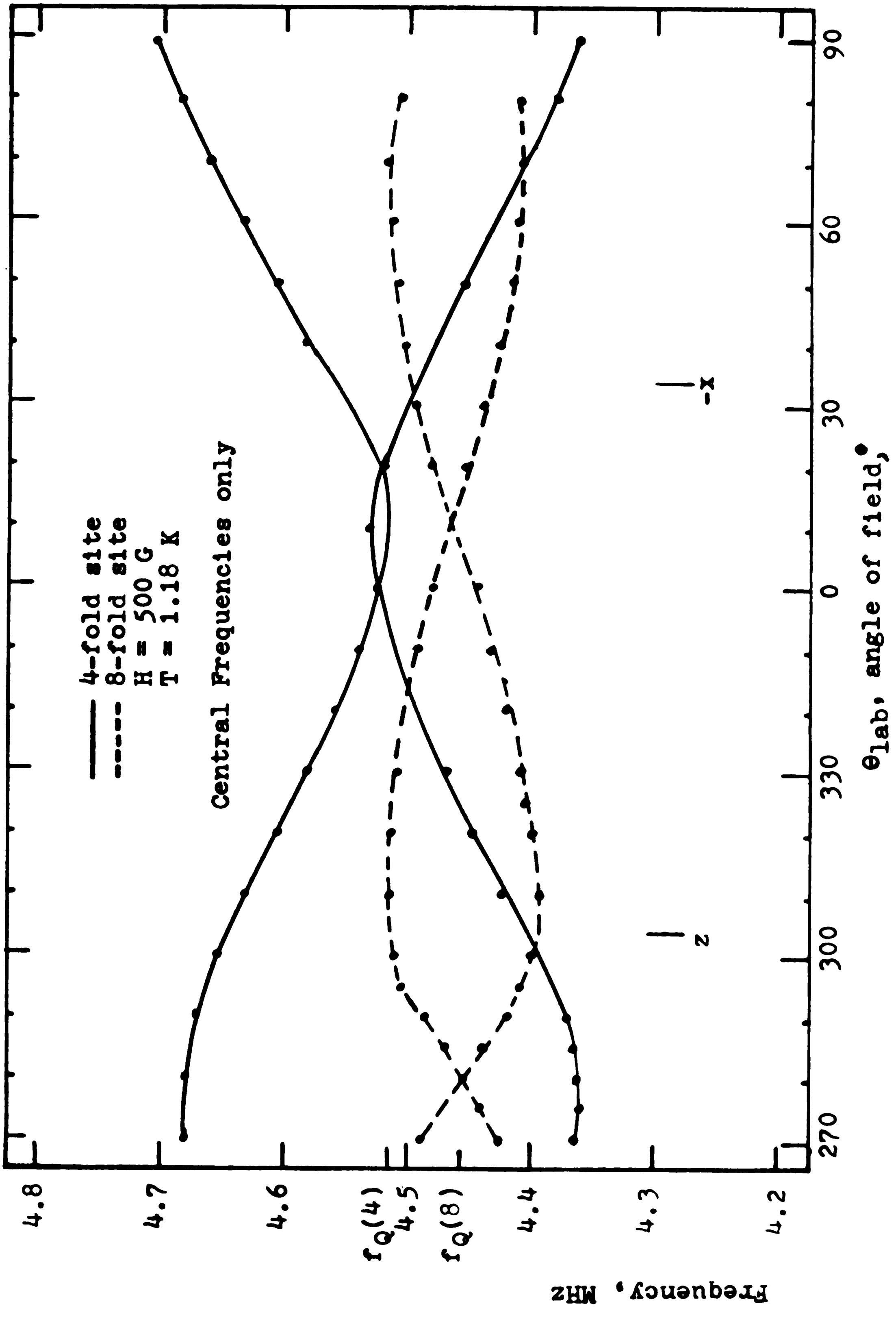

Figure 8: H in xz principal axis plane, 8-fold site

VII DATA DIAGRAMS AND INTERPRETATION

As datum was recorded in the data book, it was also plotted on graph paper, frequency vs. lab angle. The first step in the analysis consisted in connecting the data points, usually at 5° intervals, by curves. Next, approximate symmetries of these curves about the two pure quadrupole frequencies were noted, and the curves thus identified by site.

For purposes of fitting, data that had been organized by site was transferred to computer punch cards, which contained the two lab angles, the four recorded frequencies belonging to that particular site at this orientation, signal strength symbols and site number.

There now follows a description of some representative data plots:

Figure 5: H in cleavage plane of the four-fold site. The four-fold and eight-fold sites are easily distinguished by noting their symmetries about the respective pure quadrupole frequencies f_Q. Maximum splitting of lines occurs in the y principal axis direction. It is seen that the y axes of the four-fold site and the two eight-fold sites are separated by 60°, indicating the approximate three-fold axis of symmetry (since the y axis is two-fold).

Figure 6: H in xz principal axis plane, four-fold site. Principal axes of the crystal are as indicated. The two

crossing points of the two inner four-fold site lines, used in hand-fitting the $\underline{\underline{T}}$ tensor, are obvious. Frequencies of the two eight-fold sites coalesce in this plane.

Figure 7: H in plane $\perp$ cleavage, containing the y principal axis of the four-fold site. The two eight-fold site lines are again distinguishable.

Figure 8: H in the xz plane of the eight-fold site. Central lines only are shown. Now the eight-fold curves strongly resemble the four-fold curves of Figure 6, and the four-fold curves resemble the eight-fold curves of that same figure. This is with the goniometer rotated 60° from the position it was in when the data shown in Figure 6 was recorded, thus further indicating the existence of an approximate three-fold axis of symmetry perpendicular to the cleavage plane.

VIII FITTING THE TENSOR

Approximate Fit by Perturbation Theory

Since the data at 500 G shows only a small deviation from symmetry about the pure quadrupole frequency, it was decided that the simpler equations of perturbation theory would yield sufficient information for a first approximation to $\underline{\underline{T}}$. The results from this approximation could then be fitted to the data using more powerful methods. The equations of perturbation theory are given in the second part of Appendix A.

One modification must be made in attempting to describe the transition frequencies by perturbation theory. This theory assumes that the nuclei in a crystal see a magnetic field which is equal in magnitude and direction to the applied field. The inclusion of the dipole-dipole interaction and transferred hyperfine effect changes this picture. With the inclusion of these effects, the nuclei in the crystal see a magnetic field which differs in magnitude and direction from the applied field; it is this internal magnetic field H_i that must be used in the equations of perturbation theory.

The data from the rotation of the applied field H in the xz plane of the four-fold site (see Figure 6 and Data Table 13, Appendix D) indicates two positions where the two middle transition frequencies f_2 and f_3 are equal. Denoting these two angles by θ_{L1} and θ_{L2}, one obtains values for f_1, f_2, f_3, and f_4 at each of these angles ($f_1 > f_2 > f_3 > f_4$).

Defining θ and ϕ as the spherical polar angles between the internal field and the principal axes of the crystal, one sees that, because the xz plane is a mirror plane, $\phi = 0$ for H applied in the xz plane. One may express the θ dependence of H_i in terms of the applied field $\underline{H}$ and the magnet angle θ_L by means of the tensor $\underline{\underline{T}}$:

$$\underline{H_i} = \underline{\underline{T}} \cdot \underline{H} \tag{42}$$

or

$$|H_i| \begin{bmatrix} \sin\theta \\ 0 \\ \cos\theta \end{bmatrix} = \begin{bmatrix} T_{11} & 0 & T_{13} \\ 0 & T_{22} & 0 \\ T_{31} & 0 & T_{33} \end{bmatrix} \begin{bmatrix} \sin\theta_L \\ 0 \\ \cos\theta_L \end{bmatrix} |H| \tag{43}$$

One assumes that $T_{12} = T_{21} = T_{32} = T_{23} = 0$ because of the fact that the xz plane of the crystal is a mirror plane. Matrix multiplication yields

$$\left|\frac{H_i}{H}\right| \sin\theta = T_{11}\sin\theta_L + T_{13}\cos\theta_L \tag{44}$$

and

$$\left|\frac{H_i}{H}\right| \cos\theta = T_{13}\sin\theta_L + T_{33}\cos\theta_L \tag{45}$$

Note that data from the xz plane does not allow a determination of T_{22}.

From Appendix A, equations (A55-A58),

$$f_1 = f_Q + (\gamma\hbar H_i/2h)\{[3/2] + [1/2]\} \tag{46}$$

$$f_2 = f_Q + (\gamma\hbar H_i/2h)\{[3/2] - [1/2]\} \tag{47}$$

$$f_3 = f_Q - (\gamma\hbar H_i/2h)\{[3/2] - [1/2]\} \tag{48}$$

$$f_4 = f_Q - (\gamma\hbar H_i/2h)\{[3/2] + [1/2]\} \tag{49}$$

where f_Q is the pure quadrupole frequency. Here, as in equation (A40),

$$[m] = [a_m{}^2\cos^2\theta + (b_m{}^2 + c_m{}^2 + 2b_mc_m\cos2\phi)\sin^2\theta]^{\frac{1}{2}}. \qquad (50)$$

The constants are defined in Appendix A, equations (A44-A48).

At either of the angles θ_{L1} or θ_{L2}, where $f_2 = f_3$, one sees by equating equation (47) and (48), that

$$[3/2] = [1/2] \qquad (51)$$

Using equation (50), and solving for the angle θ in terms of the constants, one has

$$\tan^2\theta = \frac{(a_{1/2})^2 - (a_{3/2})^2}{(b_{3/2} + c_{3/2})^2 - (b_{1/2} + c_{1/2})^2} \quad . \qquad (52)$$

Evaluating the constants yields θ, the azimuthal angle of the internal field H_i in the principal axes system of the crystal.

Subtracting equations (46) and (49), and solving for H_i, one finds

$$H_i = (f_1-f_4)/(\gamma\hbar([3/2]+ [1/2])). \qquad (53)$$

By inserting the above calculated value of θ into the bracketed expressions in the denominator of equation (53), and evaluating f_1, f_4, and θ_{L1} from the data, one obtains a value for H_i. Using the other crossing point of f_2 and f_3 at a magnet angle θ_{L2}, one obtains a second value of the internal field, H_i. One may insert each of the two sets of values of θ_L and H_i into equations (44) and (45) to obtain four equations in the four unknowns T_{11}, T_{13}, T_{31}, T_{33}. The applied field H is known. Using data from Data Table 13, one obtains the solutions

$$T_{11} = 0.91 \qquad T_{13} = -0.04$$
$$T_{31} = -0.29 \qquad T_{33} = 0.26 \ , \tag{54}$$

or

$$T_{11} = -0.91 \qquad T_{13} = 0.04$$
$$T_{31} = -0.29 \qquad T_{33} = 0.26 \tag{55}$$

The first of these solutions was taken to be the correct one.

In equation (43), the direction of H_i is expressed in angles measured in the principal axis system of the crystal; hence, the tensor as derived is also expressed in the principal axis system, and may be interpreted as bringing about a transformation of the applied field from the lab to the principal axis system.

T_{22} may be determined from the data of either the xy or yz four-fold site planes. The previously described method is again used, with only one unknown. One obtains $T_{22} = 0.968$. Thus, a first approximation to $\underline{\underline{T}}$ is

$$\underline{\underline{T}}_{PA} = \begin{bmatrix} 0.91 & 0 & -0.04 \\ 0 & 0.968 & 0 \\ -0.29 & 0 & 0.259 \end{bmatrix} \tag{56}$$

Computer Fit

Because the perturbation theory used to approximate the $\underline{\underline{T}}$ tensor cannot describe the asymmetric frequency splitting observed in the laboratory, an analytical method more powerful than perturbation theory is needed. The availability of computer program subroutines which calculate nuclear quadrupole resonance frequencies exactly by finding the eigenvalues of the Hamiltonian permits a much more accurate fitting of the tensor to the data.[12]

A computer program EYEBAL was written for the CDC 6500 computer. The main function of this program is, briefly, to rotate the applied magnetic field through 180° (in steps of 5°) through some plane in the crystal whose orientation with the principal axes of the crystal is given by the angles Euler1 and Euler2. At each 5° point:

1.) The applied field is expressed in a lab-centered cartesian coordinate system.

2.) This lab field is expressed in the principal axis frame of the crystal.

3.) This applied field is then multiplied by $\underline{\underline{T}}$, also in the principal axis system.

4.) The product, the internal field, is expressed in spherical polar coordinates.

5.) The four highest nuclear quadrupole resonance frequencies for I = 3/2 are then calculated using subroutines ZEEMAN and HERDAG. These frequencies are indexed and stored in an array.

When all frequencies are stored for a 180° rotation of the field through some plane of the crystal, a plotting subroutine plots the four frequencies versus the lab angle of the magnet. Additional output includes lists of the four frequencies and the lab angle of the applied field, and the components of the internal field expressed in both lab and principal axis systems.

Typically, the applied field is rotated through the xz and xy planes, and through the plane containing y and perpendicular to the cleavage plane, for a given site in the crystal. By changing Euler1 and Euler2, any orientation is possible. The tensor $\underline{\underline{T}}$ as originally derived was used as input for EYEBAL, and the output frequencies for the rotation in the xz plane compared to corresponding data. To obtain an idea of how each component of $\underline{\underline{T}}$ influenced the spectrum, 0.05 was added to each component T_{11}, T_{13}, T_{31}, and T_{33} in turn, and that modified tensor used as input for EYEBAL.

Corrections to the tensor $\underline{\underline{T}}$ were made in the following manner: Let $f(n,\theta_L)$ denote the frequency of the nth line f_n $(n = 1...4)$ at the magnet angle θ_L, as calculated by EYEBAL. Let $df(n,\theta_L)$ denote the change in frequency necessary to make the calculated frequency equal the experimental frequency. Further, let $dg_{ab}(n,\theta_L)$ denote the change in the nth frequency f_n at θ_L brought about by adding .05 to the tensor element T_{ab}. Then $df(n,\theta_L)$ should equal a linear combination of the four values of $dg_{ab}(n,\theta_L)$ produced by incrementing each of T_{11}, T_{13}, T_{31}, and T_{33} by 0.05. That is,

$$\begin{aligned} df(n,\theta_L) &= k\cdot dg_{11}(n,\theta_L) + l\cdot dg_{13}(n,\theta_L) \\ &\quad + m\cdot dg_{31}(n,\theta_L) + p\cdot dg_{33}(n,\theta_L) \ . \qquad (57) \end{aligned}$$

By choosing four different frequencies (at either the same, or different angles θ_L) one obtains four equations in the four unknowns k, l, m, and p. By choosing four strong, unblended data points in regions of the spectrum where the calculated frequencies diverge most from the data, calculating the $df(n,\theta_L)$ for these points, and treating the matrix of coefficients as a Cramer's rule problem, one easily obtains solutions on a HP9100B calculator. Solutions k, l, m, and p are multiplied by 0.05 to yield the number δ_{ab} which must be added to T_{ab} to produce the desired correction in the spectrum.

The reliability of this method having been tested, program EYEBAL was modified to read data cards which contain lab angles of the applied field, frequencies, observed strengths, and the site number (four-fold or eight-fold). These frequencies were labelled and stored in a matrix, and then recalled and subtracted from the calculated frequencies to which they correspond. This modified program, called COMPAR, provides a rapid test for the fitting of a given tensor, and its output indicates which regions of the calculated spectrum are in least agreement with data for all three rotations of the field in the crystal.

Up to this point, the choice of data points used in fitting the tensor was based upon the assigned strength symbol, as well as agreement with neighboring data points. An additional feature of program COMPAR was a confidence test which made use of the recorded strength symbols attached to each frequency when it was recorded as datum. The meaning of these symbols is given in Table 3.

The confidence test recorded

$$\mathrm{SUMSQ}(n) = \sum_{\theta_L} \frac{(f(n,\theta_L)_{\mathrm{data}} - f(n,\theta_L)_{\mathrm{calc}})^2}{(2\Delta f)^2} \qquad (58)$$

for each of the four transition frequencies of the spectrum. Here, Δf is the observational error recorded in Table 3.

Table 3

Interpretation of Strength Symbols

Symbol	Strength	df, Observational error, kHz
A	very strong	±1
B	strong, slight blend	±2
C	strong, blend	±3
D	medium	±5
E	medium, blend	±7
F	weak	±10
G	weak, blend	±12
X,Q	No data recorded	

Precision of the Measurement

Before the final value of the tensor is presented, it is pertinent to ask what the theoretical limits of precision are for this fitting procedure. Since a given datum point could be in general a function of all five elements of $\underline{\underline{T}}$, it is difficult to relate the precision of $\underline{\underline{T}}$ to observational error Δf. Fortunately, the effects of each of the diagonal elements of $\underline{\underline{T}}$ are separable from one another. By examining the four transition frequencies along the x, y, and z principal axes of the crystal, one may observe the effect of T_{11}, T_{13}, T_{31}, and T_{33}, respectively, and separate it from the effects of the other components of the tensor. Hence, one may express the uncertainty in a particular element of $\underline{\underline{T}}$ as a function of the uncertainty in measuring a particular frequency.

The following method was used: once $\underline{\underline{T}}$ had been fitted to nearly its final form (its goodness of fit being judged by the credibility test previously described), the tensor was again deliberately altered by adding 0.01 to each of its components, in turn, and used as input for EYEBAL. The change in the calculated frequencies from their values with the unaltered tensor were calculated at angles corresponding to the four-fold site principal axes of the crystal. The results are summarized in Table 4. Table 4, showing the change in calculated frequencies along the principal axes per change of 0.01 in the elements of $\underline{\underline{T}}$, indicates the sensitivity of this fitting procedure.

Assuming the variation in frequency to be linear with variation in T_{ab}, one may express the information in Table 4 as the change in T_{ab} necessary to change the frequency along a given axis by one kHz. Since one kHz is the optimal resolution of the spectrometer, this will give optimal error bars for T_{ab}. This is done in Table 5.

The best possible determination of each element T_{ab}, assuming strong frequencies measured along the principal axes, predicts the following uncertainties:

Element	Uncertainty
T_{11}	±0.01
T_{22}	±0.005
T_{33}	±0.005
T_{13}	±0.01
T_{31}	±0.004

The best fit obtained yields:

$$\underline{\underline{T}}_{PA} = \begin{bmatrix} 0.920\pm0.01 & 0 & -0.067\pm0.01 \\ 0 & 0.968\pm0.005 & 0 \\ -0.284\pm0.004 & 0 & 0.262\pm0.005 \end{bmatrix} \qquad (59)$$

This is $\underline{\underline{T}}$ for the four-fold site, fitted to data at 1.18 K.

Goodness of fit is illustrated in Figures 9, 10, and 11. Differences between calculated and experimental frequencies vs. lab angle are plotted for four-fold site data, with H applied in the indicated planes.

Table 4

Change in calculated frequencies per change of 0.01 in T_{ab}

Element	Axis	df_1	df_2	df_3	df_4
T_{11}	x	2.1	1.5	-0.9	-1.4
	y	0	0	0	0
	z	0	0	0	0
T_{22}	x	0	0	0	0
	y	3.2	2.3	-1.9	-2.8
	z	0	0	0	0
T_{33}	x	0	0	0	0
	y	0	0	0	0
	z	3.9	2.2	-2.1	-3.8
T_{13}	x	0	0	0	0
	y	0	0	0	0
	z	-0.7	0.6	-0.7	0.7
T_{31}	x	-2.8	2.4	-2.4	2.8
	y	0	0	0	0
	z	0	0	0	0

Table 5

T_{ab} per one kHz change in f_n along a given axis

Element	Axis	f_1	f_2	f_3	f_4
T_{11}	x	0.005	0.007	-0.01	-0.007
T_{22}	y	0.003	0.004	-0.005	-0.004
T_{33}	z	0.003	0.005	-0.005	-0.003
T_{13}	z	-0.014	0.017	-0.014	0.014
T_{31}	x	-0.004	0.004	-0.004	0.004

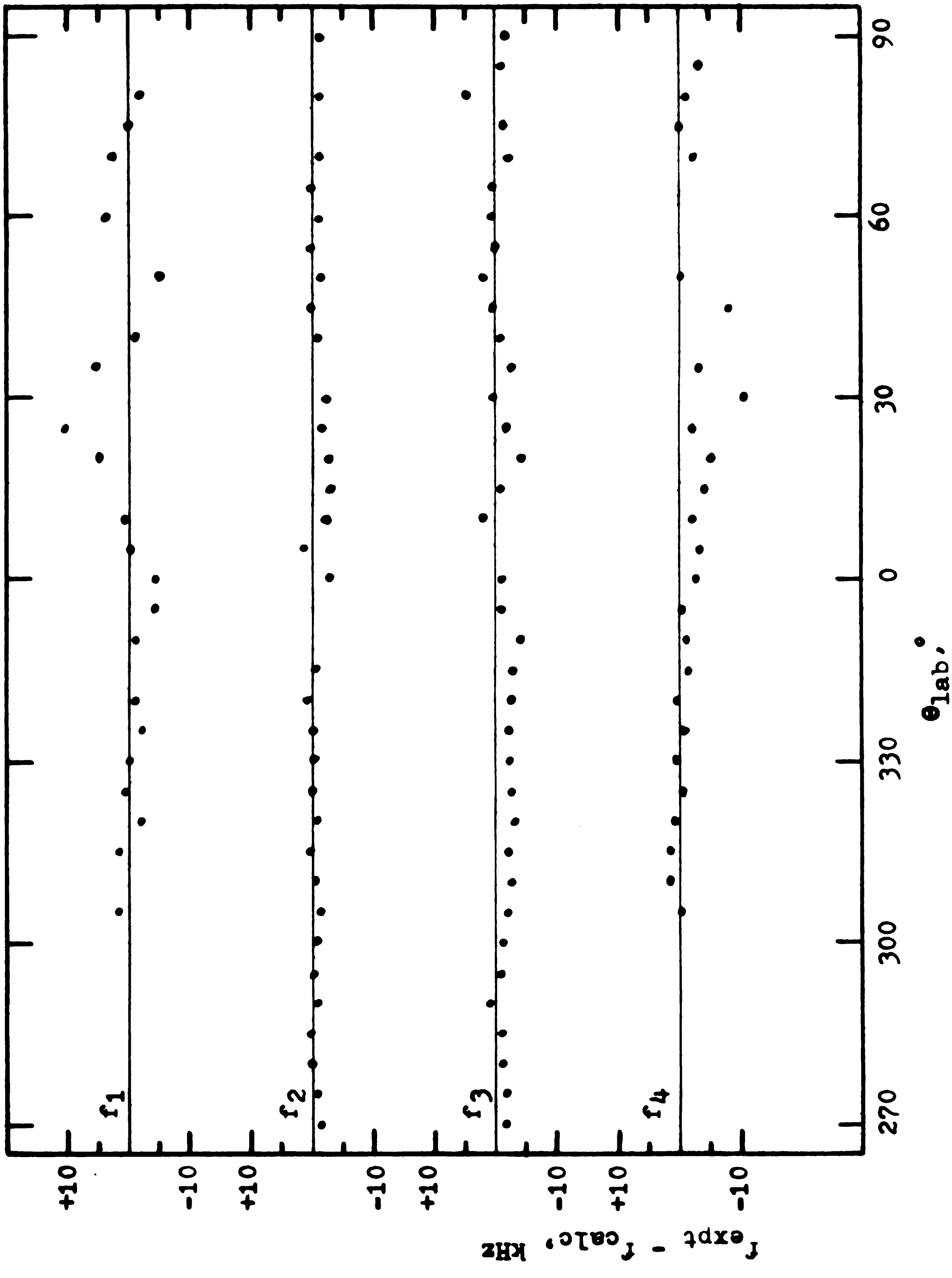

Figure 9: Goodness of fit, H in xz plane, 4-fold site

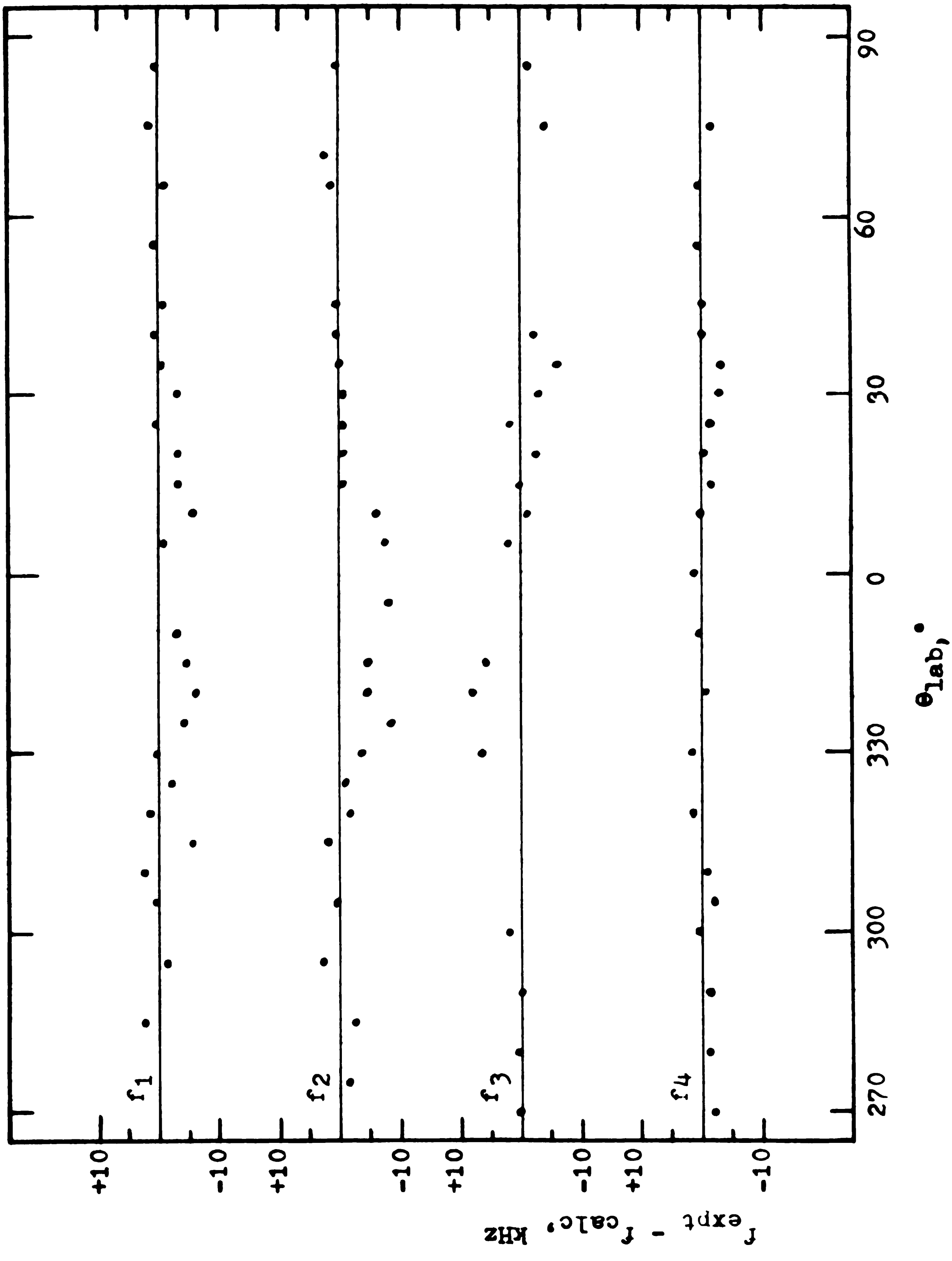

Figure 10: Goodness of fit, H in plane ⊥ cleavage, containing y, 4-fold site

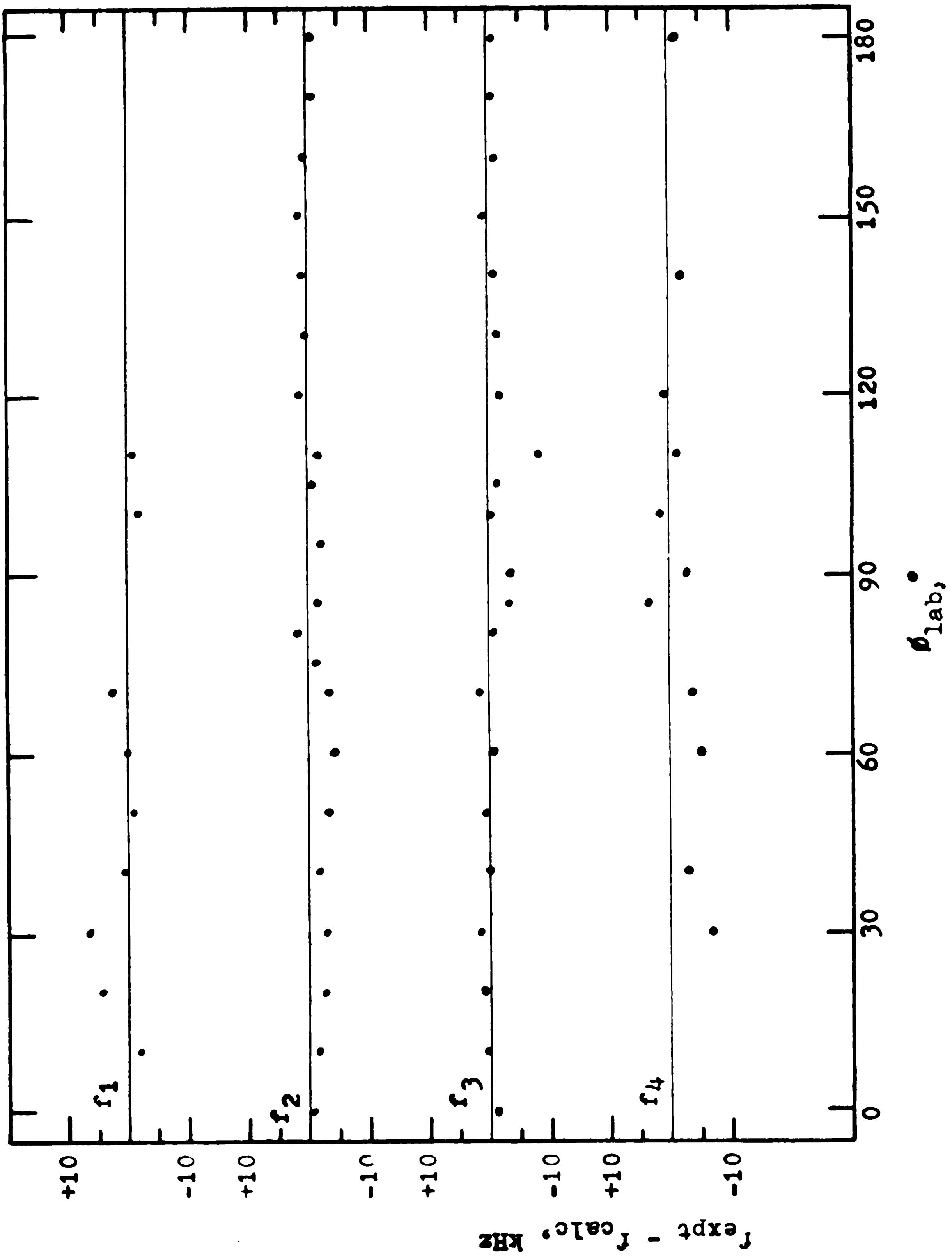

Figure 11: Goodness of fit, H in cleavage plane

IX DECOUPLING

From the theory, equation (23),

$$\underline{\underline{A}} = \gamma\hbar\mu_B[\underline{\underline{D}} - N(\underline{\underline{T}} - \underline{\underline{1}})\underline{\chi}^{-1}]\cdot\underline{\underline{g}} \qquad (60)$$

Here, γ = 2624. radians/sec

$\hbar = 1.05 \times 10^{-27}$ erg-sec

$\mu_B = 0.927 \times 10^{-20}$ erg/gauss

$N = 6.022 \times 10^{23}$ /mole

$\underline{\underline{T}}$ = the effective field tensor

χ^{-1} is the inverse susceptibility tensor

$\underline{\underline{g}}$ is the electron g-tensor

$\underline{\underline{D}}$ is the dipole-dipole interaction tensor

χ^{-1} and $\underline{\underline{g}}$ have been measured by Fairall, <u>et</u> <u>al</u>.[4] $\underline{\underline{D}}$ is evaluated by direct summation over lattice sites within a sphere of radius 100 A. Computer program YDIP evaluates $\underline{\underline{D}}$ by evaluating

$$\underline{\underline{D}} = \sum_j \frac{1 - 3(\hat{\mu}_N\cdot\hat{r}_j)^2}{r_j^3} \qquad (61)$$

by components, where the summation was over all Er lattice sites within the sphere of radius 100 A.

$$\underline{\underline{D}} = \begin{bmatrix} -0.019091 & 0 & 0.000879 \\ 0 & -0.019580 & 0 \\ 0.000879 & 0 & 0.038671 \end{bmatrix} \times 10^{24}\ \mathrm{cm}^{-3}. \qquad (62)$$

Fairall, <u>et</u> <u>al</u>., have measured $\underline{\underline{g}}$ and χ^{-1} for $ErCl_3$ in directions perpendicular and parallel to the cleavage plane, with zero applied field, from temperatures of 4 K to 0.03 K. At 1.18 K, the parallel component $\chi_{\parallel}^{-1} = 0.40$ mole/cm^3, and $\chi_{\perp}^{-1} = 1.15$ mole/cm^3. For purposes of decoupling the transferred hyperfine tensor, the inverse susceptibility must be expressed as a tensor in lab coordinates (X,Y,Z), with Z being the axis perpendicular to the cleavage plane. Fairall, et al. do not specify the orientation of the y principal axis of the crystal, which lies somewhere in the cleavage plane. Hence, one may not assign exact values to the X and Y components of $\underline{\underline{\chi}}^{-1}$. But if one assumes that the value of $\chi_{\parallel}^{-1}$ is the average of the X and Y components of $\underline{\underline{\chi}}^{-1}$, one may write

$$\underline{\underline{\chi}}_{\text{lab}}^{-1} = \begin{bmatrix} 0.40 & 0 & 0 \\ 0 & 0.40 & 0 \\ 0 & 0 & 1.15 \end{bmatrix} \qquad (63)$$

This assumption is a reasonable one. Garton, et al.,[13] measure $\underline{\underline{g}}$ values for $ErCl_3$ in host lattices of YCl_3 and $LuCl_3$ and find that the $\underline{\underline{g}}$ values in the X and Y directions are within 5% of each other. Because $\underline{\underline{\chi}}$ is a function of $\underline{\underline{g}}^2$, it follows that the X and Y components of $\underline{\underline{\chi}}$, hence $\underline{\underline{\chi}}^{-1}$, may be assumed equal as an approximation. For consistency, however, $\underline{\underline{g}}$ values quoted by Fairall, et al., are used.

$$\underline{\underline{g}} = \begin{bmatrix} 8.36 & 0 & 0 \\ 0 & 8.36 & 0 \\ 0 & 0 & 4.77 \end{bmatrix} \qquad (64)$$

Taking the best fitted value of $\underline{\underline{T}}$ and transforming into the lab system via the similarity transformation

$$\underline{\underline{T}}_{LAB} = \underline{\underline{R}}(56°)\underline{\underline{T}}_{PA}\underline{\underline{R}}^{-1}(56°), \qquad (65)$$

where $\underline{\underline{R}}$ is given by

$$\underline{\underline{R}}(\alpha) = \begin{bmatrix} \cos(\alpha) & 0 & \sin(\alpha) \\ 0 & 1 & 0 \\ -\sin(\alpha) & 0 & \cos(\alpha) \end{bmatrix} . \qquad (66)$$

One obtains $\underline{\underline{T}}_{lab}$. Using equation (60), one obtains $\underline{\underline{A}}_{lab}$, in units of ergs. In this work, energy units of cm^{-1} will be used. Hence, using a conversion factor of 1 erg = 5.035×10^{15} cm^{-1},

$$\underline{\underline{A}}_{lab} = \begin{bmatrix} 15.9 & 0 & 5.61 \\ 0 & -1.28 & 0 \\ 9.10 & 0 & 7.60 \end{bmatrix} \times 10^{-4} cm^{-1}. \qquad (67)$$

Transforming to the principal axis system,

$$\underline{\underline{A}}_{PA} = \begin{bmatrix} 3.39 & 0 & -0.637 \\ 0 & -1.28 & 0 \\ 2.86 & 0 & 20.15 \end{bmatrix} \times 10^{-4} cm^{-1}. \qquad (68)$$

Results are quoted to three significant figures. The main limitation here is that χ^{-1} must be read from a graph, and in the case of $\chi\ ^{-1}$, it is quite difficult to do this beyond two significant figures. Hence, the numbers quoted here are accurate to three significant figures at best.

Recalling that each Cl^- sees two nearest neighbor Er^{3+} ions, and since each Er^{3+} creates a hole in the Cl^- 3s and 3p orbitals, the $\underline{\underline{A}}$ tensor above must be separated into two tensors, $\underline{\underline{A}}_1$ and $\underline{\underline{A}}_2$, one for the contribution from each Er^{3+} ion.

$$\underline{\underline{A}}_1 + \underline{\underline{A}}_2 = \underline{\underline{A}}_{PA}. \qquad (69)$$

Because the xz plane is a mirror plane, these two tensors are equal in the Er system of axes (x', y', z'), with the x' axis lying along the Er-Cl internuclear radius:

$$\underline{\underline{A}}_{1\mathrm{Er}} = \underline{\underline{A}}_{2\mathrm{Er}} = \underline{\underline{A}}_{\mathrm{Er}}. \qquad (70)$$

Finally, one sees that for a bond angle θ,

$$\underline{\underline{A}}_{1\mathrm{Er}} = \underline{\underline{S}}(\tfrac{\theta}{2})\underline{\underline{A}}_{1}\underline{\underline{S}}^{-1}(\tfrac{\theta}{2}) \qquad (71)$$

and

$$\underline{\underline{A}}_{2\mathrm{Er}} = \underline{\underline{S}}(-\tfrac{\theta}{2})\underline{\underline{A}}_{2}\underline{\underline{S}}^{-1}(-\tfrac{\theta}{2}) \ . \qquad (72)$$

Here, $\underline{\underline{S}}(\alpha)$ is given by

$$\underline{\underline{S}}(\alpha) = \begin{bmatrix} \cos(\alpha) & \sin(\alpha) & 0 \\ -\sin(\alpha) & \cos(\alpha) & 0 \\ 0 & 0 & 1 \end{bmatrix} \qquad (73)$$

Inserting $\underline{\underline{A}}_{1\mathrm{Er}}$ and $\underline{\underline{A}}_{2\mathrm{Er}}$ from equations (71) and (72) into equation (70), and solving for $\underline{\underline{A}}_{2\mathrm{PA}}$ by matrix multiplication, (using the identity $\underline{\underline{S}}(\frac{\theta}{2}) = \underline{\underline{S}}^{-1}(-\frac{\theta}{2})$), one finds

$$\underline{\underline{A}}_{2\mathrm{PA}} = \underline{\underline{S}}(\tfrac{\theta}{2})\underline{\underline{S}}(\tfrac{\theta}{2})\underline{\underline{A}}_{1\mathrm{PA}}\underline{\underline{S}}^{-1}(\tfrac{\theta}{2})\underline{\underline{S}}^{-1}(\tfrac{\theta}{2}), \qquad (74)$$

Thus, using equation (69), one obtains

$$\underline{\underline{A}}_{\mathrm{PA}} = \underline{\underline{A}}_{1\mathrm{PA}} + \underline{\underline{S}}(\tfrac{\theta}{2})\underline{\underline{S}}(\tfrac{\theta}{2})\underline{\underline{A}}_{1\mathrm{PA}}\underline{\underline{S}}^{-1}(\tfrac{\theta}{2})\underline{\underline{S}}^{-1}(\tfrac{\theta}{2}). \qquad (75)$$

Multiplying matrices and equating elements of the matrices on the two sides of the equation, one obtains nine equations in nine unknowns, the unknowns being the nine elements of $\underline{\underline{A}}_{1\mathrm{PA}}$. The algebraic solutions are:

$$(A_{1\mathrm{PA}})_{11} = (A_{\mathrm{PA}})_{11}/2 \qquad (76)$$

$$(A_{1\mathrm{PA}})_{22} = (A_{\mathrm{PA}})_{22}/2 \qquad (77)$$

$$(A_{1\mathrm{PA}})_{33} = (A_{\mathrm{PA}})_{33}/2 \qquad (78)$$

$$(A_{1\mathrm{PA}})_{13} = (A_{\mathrm{PA}})_{13}/2 \qquad (79)$$

$$(A_{1\mathrm{PA}})_{31} = (A_{\mathrm{PA}})_{31}/2 \qquad (80)$$

$$(A_{1PA})_{23} = [(A_{PA})_{23}\tan(\tfrac{\theta}{2})]/2 \qquad (81)$$

$$(A_{1PA})_{32} = [(A_{PA})_{32}\tan(\tfrac{\theta}{2})]/2 \qquad (82)$$

$$(A_{1PA})_{12} = (A_{1PA})_{21} = [(A_{PA})_{11} - (A_{PA})_{22}] \cdot \frac{\sin(\frac{\theta}{2})\cos(\frac{\theta}{2})}{2(\cos^2(\frac{\theta}{2}) - \sin^2(\frac{\theta}{2}))} \; . \qquad (83)$$

One thus solves for $\underline{\underline{A}}_{1PA}$.

$\underline{\underline{A}}_{1PA}$ must now be rotated into $\underline{\underline{A}}_{1Er}$, using equation (71). The result is

$$\underline{\underline{A}}_{Er} = \underline{\underline{A}}_{1Er} = \begin{bmatrix} -8.41 & 0 & -0.483 \\ 0 & 9.47 & 0 \\ 2.17 & 0 & 10.1 \end{bmatrix} \times 10^{-4}\text{cm}^{-1} \; . \qquad (84)$$

This is the transferred hyperfine tensor at 1.18 K of $ErCl_3$, measured in the coordinate system centered on the Cl^- ion, whose x' axis lies along the internuclear radius. In the lab system of axes, this tensor measures

$$\underline{\underline{A}}_{1lab} = \begin{bmatrix} 7.97 & -3.60 & 2.80 \\ -5.26 & -0.64 & 7.14 \\ 4.55 & 8.26 & 3.80 \end{bmatrix} \times 10^{-4}\text{cm}^{-1} \; . \qquad (85)$$

There now follows a summary of all tensors used in calculations, given in both the lab and principal axis frames.

Lab Coordinate System

$$\underline{\underline{T}} = \begin{bmatrix} 0.305 & 0 & -0.131 \\ 0 & 0.968 & 0 \\ -0.348 & 0 & 0.877 \end{bmatrix} \text{(dimensionless)} \qquad (86)$$

Lab Coordinate System, Continued.

$$\underline{\underline{D}} = \begin{bmatrix} -0.0191 & 0 & 0.000879 \\ 0 & -0.01958 & 0 \\ 0.000879 & 0 & 0.03867 \end{bmatrix} \times 10^{24}\text{cm}^{-3} \qquad (87)$$

$$\underline{\underline{\chi}}^{-1} = \begin{bmatrix} 0.40 & 0 & 0 \\ 0 & 0.40 & 0 \\ 0 & 0 & 1.15 \end{bmatrix} \text{mole-cm}^{-3} \qquad (88)$$

$$\underline{\underline{\chi}} = \begin{bmatrix} 2.5 & 0 & 0 \\ 0 & 2.5 & 0 \\ 0 & 0 & 0.87 \end{bmatrix} \text{cm}^{3}\text{-mole}^{-1} \qquad (89)$$

$$\underline{\underline{g}} = \begin{bmatrix} 8.36 & 0 & 0 \\ 0 & 8.36 & 0 \\ 0 & 0 & 4.77 \end{bmatrix} \qquad (90)$$

$$\underline{\underline{g}}^{-1} = \begin{bmatrix} 0.120 & 0 & 0 \\ 0 & 0.120 & 0 \\ 0 & 0 & 0.210 \end{bmatrix} \qquad (91)$$

$$\underline{\underline{A}} = \begin{bmatrix} 15.9 & 0 & 5.61 \\ 0 & -1.28 & 0 \\ 9.10 & 0 & 7.60 \end{bmatrix} \times 10^{-4}\text{cm}^{-1} \qquad (92)$$

$$\underline{\underline{A}}_{1\text{Er}} = \begin{bmatrix} 7.97 & -3.60 & 2.80 \\ -5.26 & -0.638 & 7.14 \\ 4.55 & 8.26 & 3.80 \end{bmatrix} \times 10^{-4}\text{cm}^{-1} \qquad (93)$$

Principal Axis Coordinate System

$$\underline{\underline{T}} = \begin{bmatrix} 0.920 & 0 & -0.067 \\ 0 & 0.968 & 0 \\ -0.284 & 0 & 0.262 \end{bmatrix} \text{(dimensionless)} \qquad (94)$$

$$\underline{\underline{D}} = \begin{bmatrix} 0.0198 & 0 & -0.0271 \\ 0 & -0.0196 & 0 \\ -0.0271 & 0 & -0.000214 \end{bmatrix} \times 10^{24}\text{cm}^{-3} \qquad (95)$$

$$\underline{\underline{\chi}}^{-1} = \begin{bmatrix} 0.92 & 0 & -0.35 \\ 0 & 0.40 & 0 \\ -0.35 & 0 & 0.63 \end{bmatrix} \text{mole-cm}^{-3} \qquad (96)$$

$$\underline{\underline{\chi}} = \begin{bmatrix} 1.4 & 0 & 0.76 \\ 0 & 2.5 & 0 \\ 0.76 & 0 & 2.0 \end{bmatrix} \text{cm}^{3}\text{-mole}^{-1} \qquad (97)$$

$$\underline{\underline{g}} = \begin{bmatrix} 5.89 & 0 & 1.66 \\ 0 & 8.36 & 0 \\ 1.66 & 0 & 7.24 \end{bmatrix} \qquad (98)$$

$$\underline{\underline{g}}^{-1} = \begin{bmatrix} 0.182 & 0 & -0.042 \\ 0 & 0.120 & 0 \\ -0.042 & 0 & 0.148 \end{bmatrix} \qquad (99)$$

$$\underline{\underline{A}} = \begin{bmatrix} 3.39 & 0 & -0.637 \\ 0 & -1.28 & 0 \\ 2.86 & 0 & 20.2 \end{bmatrix} \times 10^{-4}\text{cm}^{-1} \qquad (100)$$

Principal Axis System Continued.

$$\underset{=}{A}_{\substack{1Er\\PA}} = \begin{bmatrix} 1.70 & -8.86 & -0.318 \\ -8.86 & -0.638 & -0.363 \\ 1.43 & 1.63 & 10.1 \end{bmatrix} \times 10^{-4}\mathrm{cm}^{-1} \qquad (101)$$

Again, in the Er system of axes,

$$\underset{=}{A}_{Er} = \begin{bmatrix} -8.41 & 0 & -0.483 \\ 0 & 9.47 & 0 \\ 2.17 & 0 & 10.1 \end{bmatrix} \times 10^{-4}\mathrm{cm}^{-1} \ . \qquad (102)$$

X MAGNITUDE OF THE INTERNAL FIELD

The result of the transferred hyperfine effect and dipole-dipole interaction altering the applied field at the Cl^- ion can be best shown by graphs of the internal magnetic field vs. orientation with the crystal principal axes. To this end, program EYEBAL was used with the best-fitted effective field tensor $\underline{\underline{T}}$ as input, with an applied field of 500 G being rotated through the principal axis planes of the four-fold site. The magnitude of the internal field was then plotted vs. the angle of the applied field, and the positions of the principal axes indicated. This output is tabulated in Tables 6, 7, and 8, and plotted in Figures 12, 13, and 14.

The forms of these curves were checked against output of a previous program, HINT, which used actual data taken at 1.18 K and 500 G applied field. This program used the Parker and Spence method of moments[14] and the equations of perturbation theory to calculate the internal field. Results are in complete agreement.

The results show that the internal field nearly equals the applied field along the x and y principal axes, but is reduced to nearly 25% of the applied field strength along the z axis. The contribution of the transferred hyperfine effect to this change in internal field can be found by considering the effective field tensor $\underline{\underline{T}}$. By equation (18), the effective

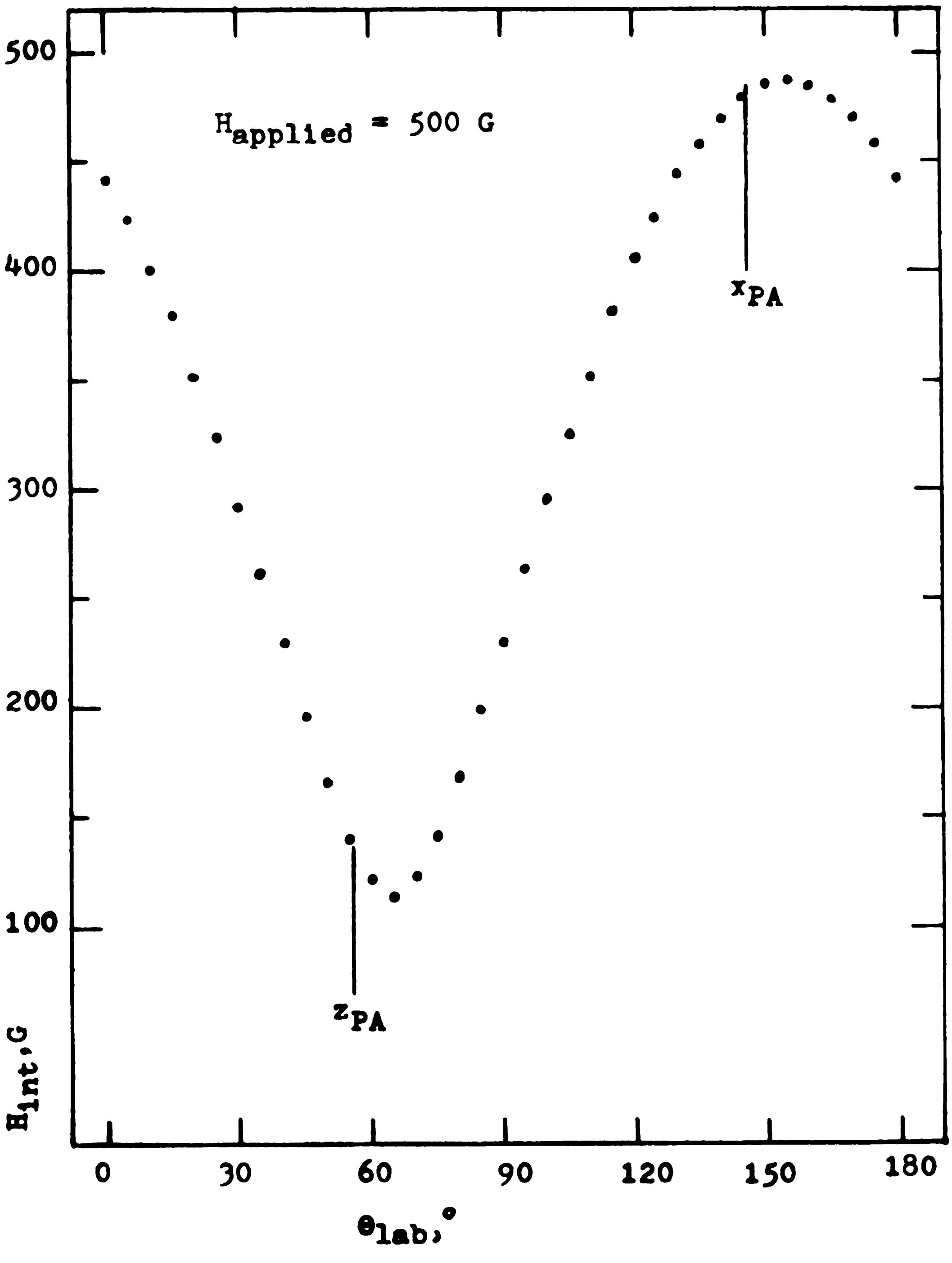

Figure 12: Internal field in xz plane, 4-fold site

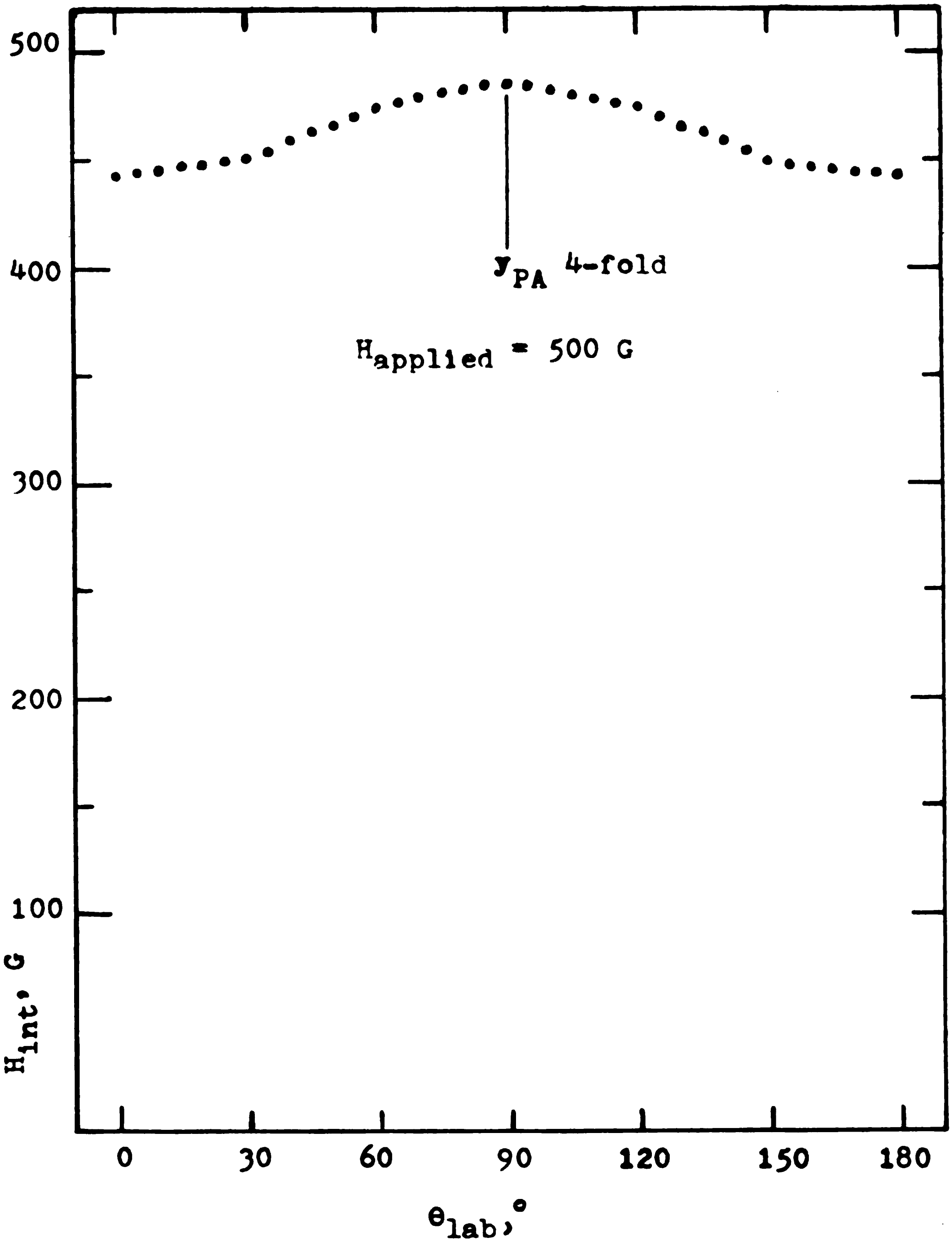

Figure 13: Internal field in plane ∥ y axis, ⊥ cleavage

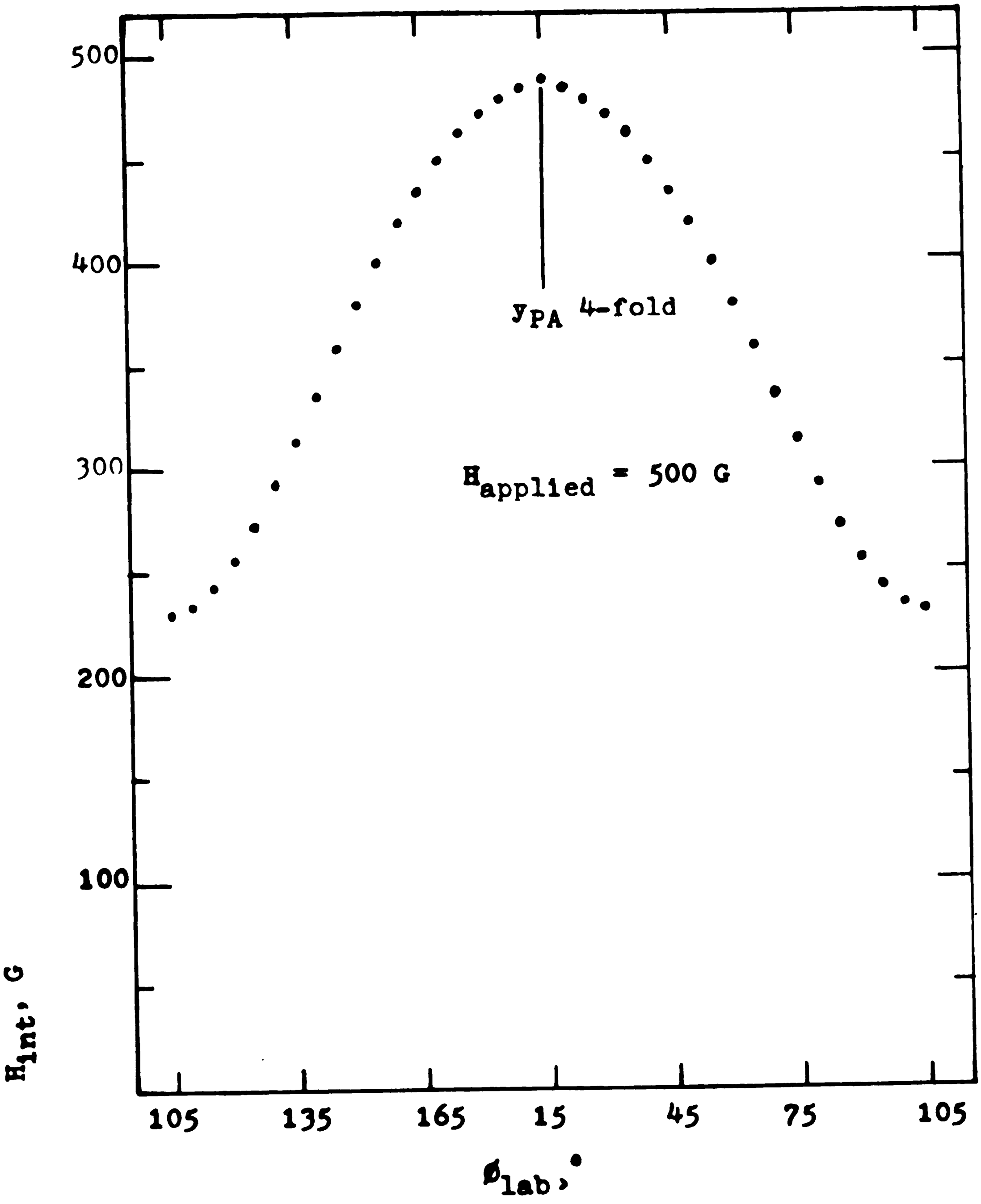

Figure 14: Internal field in cleavage plane

field tensor is

$$\underline{\underline{T}} = \underline{\underline{1}} + \left(\underline{\underline{D}} - \frac{\underline{\underline{A}}\cdot\underline{\underline{g}}^{-1}}{\gamma\hbar\mu_B}\right)\frac{\underline{\underline{\chi}}}{N} \qquad (103)$$

$$= \underline{\underline{1}} + \frac{\underline{\underline{D}}\cdot\underline{\underline{\chi}}}{N} - \frac{\underline{\underline{A}}\cdot\underline{\underline{g}}^{-1}\cdot\underline{\underline{\chi}}}{\gamma\hbar\mu_B N} \quad . \qquad (104)$$

Substituting the actual tensors in the principal axis system,

$$\underline{\underline{T}} = \underline{\underline{1}} + \frac{1}{N}\begin{bmatrix} 0.0198 & 0 & -0.0271 \\ 0 & -0.0196 & 0 \\ -0.284 & 0 & -0.00021 \end{bmatrix} \mathrm{x}10^{24}\cdot \begin{bmatrix} 1.4 & 0 & 0.76 \\ 0 & 2.5 & 0 \\ 0.76 & 0 & 2.0 \end{bmatrix}$$

$$- \begin{bmatrix} 3.39 & 0 & -0.637 \\ 0 & -1.28 & 0 \\ 2.86 & 0 & 20.2 \end{bmatrix} \mathrm{x}\,\frac{10^{-4}}{\gamma\hbar\mu_B N} \begin{bmatrix} 0.182 & 0 & -0.042 \\ 0 & 0.120 & 0 \\ -0.042 & 0 & 0.148 \end{bmatrix} \cdot$$

$$\begin{bmatrix} 1.4 & 0 & 0.76 \\ 0 & 2.5 & 0 \\ 0.76 & 0 & 2.0 \end{bmatrix} \qquad (105)$$

$$\underline{\underline{T}} = \underline{\underline{1}} + \underbrace{\begin{bmatrix} 0.011 & 0 & -0.065 \\ 0 & -0.081 & 0 \\ -0.062 & 0 & -0.035 \end{bmatrix}}_{\text{d-d}} + \underbrace{\begin{bmatrix} -0.091 & 0 & -0.002 \\ 0 & 0.049 & 0 \\ -0.222 & 0 & -0.703 \end{bmatrix}}_{\text{trans. hyp.}} \quad . \qquad (106)$$

Therefore if H is applied along the x principal axis,

$$\underline{H}_{INT} = \underline{\underline{T}}\cdot\underline{H} = \begin{bmatrix} 1 & -0.011 & -0.091 \\ & 0 & \\ & -0.062 & -0.222 \end{bmatrix} |H| \quad . \qquad (107)$$

The transferred hyperfine field opposes the applied field, as does the dipole-dipole field. The internal field is bent toward the -z direction.

If $\underline{H}$ is applied along the y principal axis,

$$\underline{H}_{INT} = \underline{\underline{T}} \cdot \underline{H} = \begin{bmatrix} 0 \\ 1 - 0.081 + 0.049 \\ 0 \end{bmatrix} |H| \ . \qquad (108)$$

The transferred hyperfine field would add to the applied field, but is opposed by the dipole-dipole field.

If $\underline{H}$ is applied along the z principal axis,

$$\underline{H}_{INT} = \underline{\underline{T}} \cdot \underline{H} \begin{bmatrix} & - 0.065 & - 0.002 \\ & 0 & \\ 1 & - 0.035 & - 0.703 \end{bmatrix} |H| \ . \qquad (109)$$

Here, the transferred hyperfine field dominates even the applied field along the z principal axis direction, and is primarily responsible for the large observed decrease in the internal field observed along the z principal axis.

Similarly, in the lab system, substituting the tensors into equation (104),

$$\underline{\underline{T}} = \underline{\underline{1}} + \frac{1}{N} \begin{bmatrix} -0.0191 & 0 & 0.000879 \\ 0 & -0.01958 & 0 \\ 0.000879 & 0 & 0.03867 \end{bmatrix} \text{x } 10^{24} \cdot$$

$$\begin{bmatrix} 2.5 & 0 & 0 \\ 0 & 2.5 & 0 \\ 0 & 0 & 0.87 \end{bmatrix} - \begin{bmatrix} 15.9 & 0 & 5.61 \\ 0 & -1.28 & 0 \\ 9.10 & 0 & 7.60 \end{bmatrix} \text{x } \frac{10^{-4}}{\gamma \hbar \mu_B N} \cdot$$

$$\begin{bmatrix} 0.120 & 0 & 0 \\ 0 & 0.120 & 0 \\ 0 & 0 & 0.210 \end{bmatrix} \cdot \begin{bmatrix} 2.5 & 0 & 0 \\ 0 & 2.5 & 0 \\ 0 & 0 & 0.87 \end{bmatrix} . \qquad (110)$$

It should be remarked that $\underline{\underline{T}}$ was tested to determine if it correctly predicted the splitting observed at magnetic fields higher and lower than 500 G. In one experiment, the frequencies of several strong four and eight-fold site lines were measured as the applied magnetic field was varied from 250 G to 7000 G. The magnetic field was along the line of intersection of the cleavage and xz planes of the crystal. $\underline{\underline{T}}$ and the various magnitudes of H were used as input for program EYEBAL, and the calculated frequencies agreed in all cases with the data, within the accuracy of measurement for these frequencies. This justifies the fact that most data for the fitting of $\underline{\underline{T}}$ was taken at 500 G, and points to the fact that, at least at this orientation of the field, $\underline{\underline{T}}$ is field-independent.

TABLE 6

Magnitude of the internal field for 500 G applied field in xz plane of the four-fold site.

θ_{lab}, °	H_{int}, G	θ_{lab}, °	H_{int}, G
0	443.1	90	231.2
5	424.6	95	263.6
10	403.2	100	295.3
15	379.1	105	325.7
20	352.5	110	354.3
25	323.8	115	380.7
30	293.4	120	404.7
35	261.6	125	425.9
40	229.2	130	444.2
45	197.0	135	459.3
50	166.5	140	471.3
55	139.9	145	479.8
60	120.9	150	484.9
65	114.2	155	486.6
70	121.8	160	484.7
75	141.4	165	479.4
80	168.3	170	470.6
85	199.0	175	458.5
		180	443.1

TABLE 7

Magnitude of the internal field for 500 G applied field in plane perpendicular to cleavage plane and containing the y principal axis, four-fold site.

θ_{lab}, °	H_{int}, G	θ_{lab}, °	H_{int}, G
0	443.1	90	484.0
5	443.4	95	483.7
10	444.4	100	482.8
15	445.9	105	481.4
20	448.1	110	479.4
25	450.7	115	477.0
30	453.7	120	474.1
35	457.0	125	470.9
40	460.4	130	467.5
45	464.0	135	464.0
50	467.5	140	460.4
55	470.9	145	457.0
60	474.1	150	453.7
65	477.0	155	450.7
70	479.4	160	448.1
75	481.4	165	445.9
80	482.8	170	444.4
85	483.7	175	443.4
		180	443.1

TABLE 8

Magnitude of the internal field for 500 G applied field in the cleavage plane, four-fold site.

ϕ_{lab},°	H_{int},G	ϕ_{lab},°	H_{int},G
0	231.2	90	484.0
5	234.2	95	482.6
10	242.7	100	478.3
15	256.1	105	471.3
20	273.2	110	461.6
25	292.8	115	449.4
30	314.1	120	434.8
35	336.1	125	418.1
40	358.0	130	399.5
45	379.3	135	379.3
50	399.5	140	358.0
55	418.1	145	336.1
60	434.8	150	314.1
65	449.4	155	292.8
70	461.6	160	273.2
75	471.3	165	256.1
80	478.3	170	242.7
85	482.6	175	234.2
		180	231.2

XI RESULTS

From equation (84),

$$\underline{\underline{A}}_{Er} = \begin{bmatrix} -8.41 & 0 & -0.483 \\ 0 & 9.47 & 0 \\ 2.17 & 0 & 10.1 \end{bmatrix} \text{ x } 10^{-4}\text{cm}^{-1}. \qquad (111)$$

By equation (30),

$$A_S = \frac{1}{3} \sum_{x',y',z'} A_{jj} = 3.71 \text{ x } 10^{-4}\text{cm}^{-1} \qquad (112)$$

And from the requirement that $\underline{\underline{A}}_p$ be traceless,

$$\underline{\underline{A}}_{Er} = A_S\underline{\underline{1}} + \begin{bmatrix} A_{px'x'} & 0 & A_{px'z'} \\ 0 & A_{py'y'} & 0 \\ A_{pz'x'} & 0 & A_{pz'z'} \end{bmatrix} \qquad (113)$$

$$= 3.71 \text{ x } 10^{-4}\underline{\underline{1}} + \begin{bmatrix} -12.1 & 0 & -0.483 \\ 0 & 5.76 & 0 \\ 2.17 & 0 & 6.37 \end{bmatrix} \text{x } 10^{-4},\text{cm}^{-1} \qquad (114)$$

to three significant figures. Hence, by equation (37),

$$A_\sigma - A_{\pi y} = \frac{1}{3}(A_{x'x'} - A_{y'y'}) = -5.96 \text{ x } 10^{-4}\text{cm}^{-1} \qquad (115)$$

By equation (38),

$$A_\sigma - A_{\pi z} = \frac{1}{3}(A_{x'x'} - A_{z'z'}) = -6.16 \text{ x } 10^{-4}\text{cm}^{-1} \qquad (116)$$

And by equation (39),

$$A_{\pi y} - A_{\pi z} = \frac{1}{3}(A_{y'y'} - A_{z'z'}) = -0.233 \text{ x } 10^{-4}\text{cm}^{-1} \qquad (117)$$

XII CONCLUSION

The transferred hyperfine interaction tensor has been measured at 1.18 K and 500 G. It has been found that the tensor as measured is field-independent over a range of 250-7000 G. Strong temperature dependence has been suggested (Appendix B).

Plots of internal field vs. angle of applied field show the greatest modification of the applied field occurs close to the z principal axis of the crystal, where the transferred hyperfine interaction causes the internal magnetic field to drop to only 30% of the applied field value.

The transferred hyperfine interaction tensor derived (see equation (112), Section XI) has an isotropic part,

$$A_s = 3.71 \times 10^{-4} \text{ cm}^{-1} \qquad (118)$$

and an anisotropic part,

$$\underline{\underline{A}}_p = \begin{bmatrix} -12.1 & 0 & -0.483 \\ 0 & 5.76 & 0 \\ 2.17 & 0 & 6.37 \end{bmatrix} \times 10^{-4}\text{cm}^{-1} \qquad (119)$$

The pairwise differences in $\underline{\underline{A}}_p$ between σ and π orbitals are, by equations (37), (38), (39):

$$A_\sigma - A_{\pi y} = -5.96 \times 10^{-4} \text{ cm}^{-1} \qquad (120)$$

$$A_\sigma - A_{\pi z} = -6.16 \times 10^{-4} \text{ cm}^{-1} \qquad (121)$$

$$A_{\pi y} - A_{\pi z} = -0.61 \times 10^{-4} \text{ cm}^{-1} \qquad (122)$$

The interaction between the Cl^{35} nucleus and holes in both π orbitals is nearly equal. The pairwise difference $A_\sigma - A_\pi = -6. \times 10^{-4}$ cm^{-1} indicates that π bonding dominates σ bonding in $ErCl_3$. The relative magnitudes of A_s and the diagonal elements of $\underline{\underline{A}}_p$ indicates that holes in the Cl^- 3p orbitals have a greater interaction with the Cl^{35} nucleus than do holes in the 3s orbitals. This implies that the Cl^- wave function is primarily p-state in $ErCl_3$.

For a comparison between the hyperfine interaction of $ErCl_3$ and other transition metal halides, see Table 9.

TABLE 9

Magnitudes of Some Transferred Hyperfine Interactions

Compound	A_s (10^{-4} cm^{-1})	$A_\sigma - A_\pi$ (10^{-4} cm^{-1})	Ref.
$ErCl_3$	3.71	-6.	
$CuCl_2 \cdot 2H_2O$	7.8	5.0	6
$CdCl_2:Cu^{++}$	9.5	4.5	6
$CoCl_2 \cdot 2H_2O$	5.6	0.8	6
$AgCl:Fe^{3+}$	2.8	0.5	6
$CsMnCl_3$			19
Cl_{II}(linear bridge)	1.7	0.0	
Cl_I (bent bridge)	1.46	0.06	
$CsCoCl_3$ (bent bridge)	2.68	1.03	19

The small relative magnitude of the off-diagonal elements of $\underline{\underline{A}}_p$, as well as a look at the crystal structure, suggests that they may be due to errors in evaluating certain contributions to the Hamiltonian. The location of the Cl^- ion in the $ErCl_3$ crystal does not suggest that there would be any x'z' or z'x' elements in the tensor. The two-fold symmetry about the y principal axis, and the existence of the mirror plane argue against any off-diagonal elements.

In crystals such as cubic $KNiF_3$,[3,15] the existence of the four-fold axis of symmetry, the x principal axis, necessitates that there be no off-diagonal elements in $\underline{\underline{A}}_p$. Further, $A_{py'y'} = A_{pz'z'}$, hence the interactions in the Cl^- 3p(y') and 3p(z') orbitals are equal. Although one cannot invoke this four-fold symmetry in the case of $ErCl_3$, neither can one adequately explain the existence of the off-diagonal elements.

Imprecision in analysis leading to off-diagonal elements could have several causes. The quantity $\underline{\underline{\chi}}^{-1}$ used to decouple $\underline{\underline{A}}$ is the most doubtful. First of all, $\underline{\underline{\chi}}^{-1}$ was interpolated from a steeply changing curve. Secondly, the two components of $\underline{\underline{\chi}}^{-1}$ in the cleavage plane were presumed equal, and the results of Garton, _et_ _al_.,[13] dispute this. Thirdly, there is enough doubt about susceptibility measurements on $ErCl_3$ in general to cast doubt on the results of Fairall, _et_ _al_.,[4] as will now be discussed.

In discussing susceptibility measurements on $ErCl_3$, four points should be mentioned. First of all, a spherical sample should be used in order to control demagnetizing effects. Secondly, the crystal should not be stored in oil, because it readily absorbs oil between its cleavage planes, and this oil makes an accurate determination of the mass impossible. Thirdly, the temperature control must be well calibrated, and the sample in good thermal contact with the bath. This demands a small sample. Fourthly, one would ideally like to measure the susceptibility of the crystal with a magnetic field applied simultaneously in the same direction as the measurement.

The first and the second requirements are almost incompatible. It is difficult to obtain spherically shaped samples, and the only way attempted was to slowly grind the crystal under oil, which both aids the grinding and prevents the absorption of water vapor from the air. The Fairall measurement was made with a cylindrical sample, and with zero applied field.

Further, there are theoretical complications in fitting the measured susceptibility to a Curie-Weiss law. Since the electron g-value is determined from the Curie constant, this casts doubt upon the $\underline{\underline{g}}$ tensor used in decoupling $\underline{\underline{A}}$. Wolf and Heintz[16] show that for concentrated materials with appreciable interactions between the magnetic moments, there exist contributions to the g-value from cross-terms between the off-diagonal part of the magnetization and the interactions. They also suggest that one must not neglect higher order terms in the Curie-Weiss law (the second-order g-shift[17]).

Their measurements on a powdered sample of $ErCl_3$ suggest that the Curie constant may change by as much as 35% when higher-ordered terms are included.

The results of this analysis could be most improved by better susceptibility data. The fitting of the effective field tensor to the data could, however, be slightly improved by a Chi-squared fit computer program which would vary all five elements of the effective field tensor, as well as the applied field angles. Thus, the values of the transferred hyperfine interaction tensor reported here represent an estimate of a quantity that has not been previously reported on for this crystal, and give an insight into the Cl^- electronic state in $ErCl_3$.

LIST OF REFERENCES

LIST OF REFERENCES

1. A. Abragam and B. Bleaney, Paramagnetic Resonance of Transition Ions (Clarendon Press, Oxford, 1970), Chap. 1, pp. 13-15.
2. A. Narath in Hyperfine Interactions (Academic Press, New York, 1967), ed. A. Freeman and R. Frankel, Chap. 7, p. 301.
3. R. G. Shulman and S. Sugano, Phys. Rev. 130, 506 (1963).
4. C. W. Fairall, J. A. Cowen, and E. Grabowski, (to be published).
5. Narath, p. 304.
6. R. Bersohn and R. G. Shulman, J. Chem. Phys. 45, 2298 (1966).
7. E. H. Carlson and H. S. Adams, J. Chem. Phys. 51, 388 (1969).
8. R. Wyckoff, Crystal Structures (Interscience Publishers, New York, 1964), 2nd ed., Vol. 2, Chap. VB, pp. 56-57.
9. W. J. M. DeJonge, G. N. Srivastava, and Paul M. Parker, J. Chem. Phys. 49, 2843 (1968).
10. C. Dean, Phys. Rev. 96, 1053 (1954).
11. S. I. Parks, "NMR in Paramagnetic $NdBr_3$ and UI_3", dissertation, Florida State University, 1967, p. 103.
12. E. H. Carlson, "Computer Program for Nuclear Magnetic and Quadrupole Resonance Frequencies and Intensities, I = 3/2 to 9", University of Alabama, 1965.
13. G. Garton, M. T. Hutchings, R. Shore, and W. P. Wolf, J. Chem. Phys. 41, 1970 (1964).
14. Paul M. Parker and R. D. Spence, Phys. Rev. 160, 383 (1967).
15. Narath, p. 304.

16. W. P. Wolf and J. F. Heintz, J. Appl. Phys. 36, 1127 (1965).

17. M. T. Hutchings and W. P. Wolf, Phys. Rev. Letters 11, 187 (1963).

18. T. P. Das and E. L. Hahn, Nuclear Quadrupole Resonance Spectroscopy (Academic Press Inc., New York, 1958), Chap. 1, p. 1.

19. H. Rinneberg and H. Hartmann, J. Chem. Phys. 52, 5814 (1970).

APPENDICES

APPENDIX A

Diagonalizing the Quadrupole Hamiltonian

The Hamiltonian for the interaction of the quadrupole moment of a nucleus with the electric field gradient at its position due to surrounding charges is given by the tensor-scalar product[18]

$$H_Q = \underline{\underline{Q}}\cdot\underline{\underline{\nabla E}} = \sum_m Q_2^m \, (\nabla E)_2^{-m} \tag{A1}$$

where Q defines the quadrupole charge distribution in the nucleus. In terms of cartesian coordinates X, Y, Z, its irreducible components are

$$Q_2^0 = eQ \, (3I_z{}^2 - \underline{I}^2)/(2I(2I - 1)) \tag{A2}$$

$$Q_2^{\pm 1} = eQ\sqrt{6} \, (I_z I^{\pm} + I^{\pm} I_z)/(4I(2I - 1)) \tag{A3}$$

$$Q_2^{\pm 2} = eQ\sqrt{6} \, (I^{\pm})^2/(4I(2I - 1)) \tag{A4}$$

where

$$I^{\pm} = I_X \pm iI_Y. \tag{A5}$$

The scalar quadrupole moment Q of the nucleus is given by

$$eQ = \int \rho_i r_i^2 \, (3 \cos^2\theta_{iI} - 1) \, d\tau_i \tag{A6}$$

where ρ_i is the charge density in a small volume element $d\tau_i$ inside the nucleus at a distance r_i from the center, and θ_{iI} is the angle between the radius vector $\underline{r}_i$ and the nuclear spin axis. The field gradient at the nucleus is defined by the tensor $\underline{\underline{\nabla E}}$, which has nine components $-V_{ij}$, which in cartesian coordinates are

$$V_{ij} = \frac{\partial^2 V}{\partial x_i \cdot \partial x_j} \quad (x_i, x_j = X, Y, Z) \qquad \text{(A7)}$$

and V is the electrostatic potential at the nucleus due to the surrounding charges.

If Laplace's equation holds, meaning that all charges producing the electric field are external to the nucleus, then $\underline{\underline{\nabla E}}'$ is symmetric and traceless, and its five irreducible components are

$$(\nabla E')_0 = \frac{1}{2} V_{ZZ} \qquad \text{(A8)}$$

$$(\nabla E')_{\pm 1} = -(V_{XZ} \pm iV_{YZ})/\sqrt{6} \qquad \text{(A9)}$$

$$(\nabla E')_{\pm 2} = (V_{XX} - V_{YY} \pm 2iV_{XY})/(2\sqrt{6}). \qquad \text{(A10)}$$

Transforming to a set of principal axes x,y,z, the irreducible components become

$$(\nabla E)_0 = \frac{1}{2} V_{zz} = \frac{1}{2} eq \qquad \text{(A11)}$$

$$(\nabla E)_{\pm 1} = 0 \qquad \text{(A12)}$$

$$(\nabla E)_{\pm 2} = (V_{xx} - V_{yy})/(2\sqrt{6}) = \eta eq/(2\sqrt{6}) \qquad \text{(A13)}$$

and ηeq is called the quadrupole coupling constant. The asymmetry parameter η is defined by

$$\eta = \frac{V_{xx} - V_{yy}}{V_{zz}} \qquad \text{(A14)}$$

and be convention, one states

$$|V_{xx}| < |V_{yy}| < |V_{zz}| \qquad \text{(A15)}$$

in the principal axis system. Then η varies between 0 and 1. If $\eta = 0$,

$$V_{xx} = V_{yy} = -\frac{1}{2} eq \qquad \text{(A16)}$$

$$V_{zz} = eq \ . \qquad \text{(A17)}$$

If $\eta = 1$,

$$V_{xx} = 0 \qquad \text{(A18)}$$

$$V_{yy} = -V_{zz} \ . \qquad \text{(A19)}$$

One further defines the quantity

$$A = e^2qQ/(4I(2I - 1)) \ . \qquad \text{(A20)}$$

Then the quadrupole Hamiltonian is

$$\mathcal{H}_Q = A(3I_z{}^2 - \underline{I}^2) + \frac{1}{2} A(I^{\pm})^2\eta \qquad \text{(A21)}$$

If $\eta = 0$, the matrix elements are

$$\langle m|\mathcal{H}_Q|m\rangle = A(3m^2 - I(I + 1)) \ . \qquad \text{(A22)}$$

For a system of nuclear spin $I = 3/2$, in a representation in which the eigenvalues of I_z are diagonal,

$$E_Q = \begin{bmatrix} 3A & 0 & 0 & 0 \\ 0 & -3A & 0 & 0 \\ 0 & 0 & -3A & 0 \\ 0 & 0 & 0 & 3A \end{bmatrix} \qquad \text{(A23)}$$

There are two doubly degenerate energy levels +3A and -3A.

The transition frequency between these levels is $f_Q = 6A/h$. (A24)

When $\eta \neq 0$, the off-diagonal matrix elements are

$$\langle m|\mathcal{H}_Q|m{+}2\rangle = \langle m{-}2|\mathcal{H}_Q|m\rangle =$$

$$\sqrt{((I+m)(I-m+1)(I+m-1)(I-m+2))}\ A\eta/2. \qquad \text{(A25)}$$

For an $I = 3/2$ system,

$$\mathcal{H}_Q = \begin{bmatrix} 3A & 0 & \sqrt{3}\eta & 0 \\ 0 & -3A & 0 & \sqrt{3}\eta \\ \sqrt{3}\eta & 0 & -3A & 0 \\ 0 & \sqrt{3}\eta & 0 & 3A \end{bmatrix} \qquad \text{(A26)}$$

Rearranging rows and columns and block-diagonalizing, one obtains the eigenvalues

$$E_Q = \begin{bmatrix} 3A\rho & 0 & 0 & 0 \\ 0 & -3A\rho & 0 & 0 \\ 0 & 0 & -3A\rho & 0 \\ 0 & 0 & 0 & 3A\rho \end{bmatrix} \qquad \text{(A27)}$$

where

$$\rho = (1 + \eta^2/3)^{\frac{1}{2}} \ . \qquad \text{(A28)}$$

As before, there are two doubly degenerate energy levels. The transition frequency between the two levels is

$$f_Q = 6A\rho/h \ . \qquad \text{(A29)}$$

The transitions between the energy levels may be produced by the application of an oscillating magnetic field which interacts with the magnetic dipole moment of the nucleus, producing a time-dependent perturbation. A constant magnetic field H may also be applied to break up the degeneracy of the pure quadrupole levels. If the magnetic interaction is small compared to the quadrupole interaction ($\gamma\hbar H \ll e^2 qQ$) then this magnetic interaction, the Zeeman interaction, may be treated as a time-independent perturbation of the quadrupole Hamiltonian. The total Hamiltonian is then

$$\mathcal{H} = \mathcal{H}_Q + \mathcal{H}_m + \mathcal{H}'(t) \qquad \text{(A30)}$$

$$\mathcal{H}_m = -\gamma\hbar \underline{I} \cdot \underline{H} \ . \qquad \text{(A31)}$$

In terms of raising and lowering operators $I^{\pm}$, $H^{\pm}$,

$$H^{\pm} = H_x \pm iH_y \ , \qquad \text{(A32)}$$

$$\mathcal{H}_m = -\gamma\hbar H(I_z H_z + \frac{1}{2}(I^+ H^- + I^- H^+)) \qquad \text{(A33)}$$

The matrix elements of interest are

$$\langle m|I_z H_z|m\rangle = -\gamma H m \cos\theta \ , \qquad \text{(A34)}$$

and

$$\langle m|I^- H^+|m+1\rangle =$$

$$\frac{-\gamma H}{2}\ ((I-m)(I+m+1))^{\frac{1}{2}} \sin\theta\ (\cos\phi + i\sin\phi\ ) \qquad \text{(A35)}$$

where θ and ϕ are the usual spherical polar angles between the applied field and the crystal principal axes. For an $I = 3/2$ system,

$$\langle m|I^- H^+|m+1\rangle = \frac{-\gamma H}{2}\ ((3/2 - m)(5/2 + m))^{\frac{1}{2}} \ *$$

$$*\sin\theta\ (\cos\phi + i\sin\ \phi). \qquad \text{(A36)}$$

Computer subroutines ZEEMAN and HERDAG[12] were used to obtain the transition frequencies in all programs used to fit the internal field tensor $\underline{\underline{T}}$. However, for the initial fit of the tensor, the equations of perturbation theory were used.

Perturbation Theory for I=3/2 Case

For a system of nuclei of spin $I=3/2$ in a constant magnetic field H, the energy eigenvalues $E_{m,\pm}$ where m represents the limiting values of m_z, are:[10]

$$E_{3/2,\pm} = E_0 \pm (\gamma\hbar H/2)[3/2] \qquad \text{(A37)}$$

$$E_{1/2,\pm} = E_0 \pm (\gamma\hbar H/2)[1/2] \qquad \text{(A38)}$$

correct to first order in H. Here,

$$[m] = [a_m{}^2\cos^2\theta + (b_m{}^2 + c_m{}^2 + 2b_m c_m \cos 2\phi)\sin^2\theta]^{\frac{1}{2}} \qquad \text{(A39)}$$

and again, it is presumed that

$$\gamma\hbar H << e^2 qQ. \qquad \text{(A40)}$$

θ and ϕ are the orientation angles in spherical polar coordinates of the magnetic field with respect to the principal axis system of the crystal,

$$E_0 = A(1 + \eta^2/3)^{\frac{1}{2}} \qquad \text{(A41)}$$

$$A = e^2qQ/(4I(2I - 1)), \qquad \text{(A42)}$$

and

$$\eta = \frac{\frac{\partial^2 V}{\partial x^2} - \frac{\partial^2 V}{\partial y^2}}{\frac{\partial^2 V}{\partial z^2}} \qquad \text{(A43)}$$

The equations for the energy eigenvalues are true for any value of η between 0 and 1. The constants in these equations are defined as:

$$a_{3/2} = -1 - 2/\rho \qquad \text{(A44)}$$

$$a_{1/2} = -1 + 2/\rho \qquad \text{(A45)}$$

$$b_{3/2} = 1 - 1/\rho \qquad \text{(A46)}$$

$$b_{1/2} = 1 + 1/\rho \qquad \text{(A47)}$$

$$c_{3/2} = -c_{1/2} = \eta/\rho \qquad \text{(A48)}$$

$$= (1 + \eta^2/3)^{\frac{1}{2}} \qquad \text{(A49)}$$

These energy levels imply a Zeeman spectrum consisting of four frequencies symmetrically spaced about the pure quadrupole frequency. From Figure 15, it can be seen that

$$f_1 = (E_{3/2,+} - E_{1/2,-})/h \qquad \text{(A50)}$$

$$f_2 = (E_{3/2,+} - E_{1/2,+})/h \qquad \text{(A51)}$$

$$f_3 = (E_{3/2,-} - E_{1/2,-})/h \qquad \text{(A52)}$$

$$f_4 = (E_{3/2,-} - E_{1/2,+})/h \qquad \text{(A53)}$$

and

$$f_Q = 2E_0/h \qquad \text{(A54)}$$

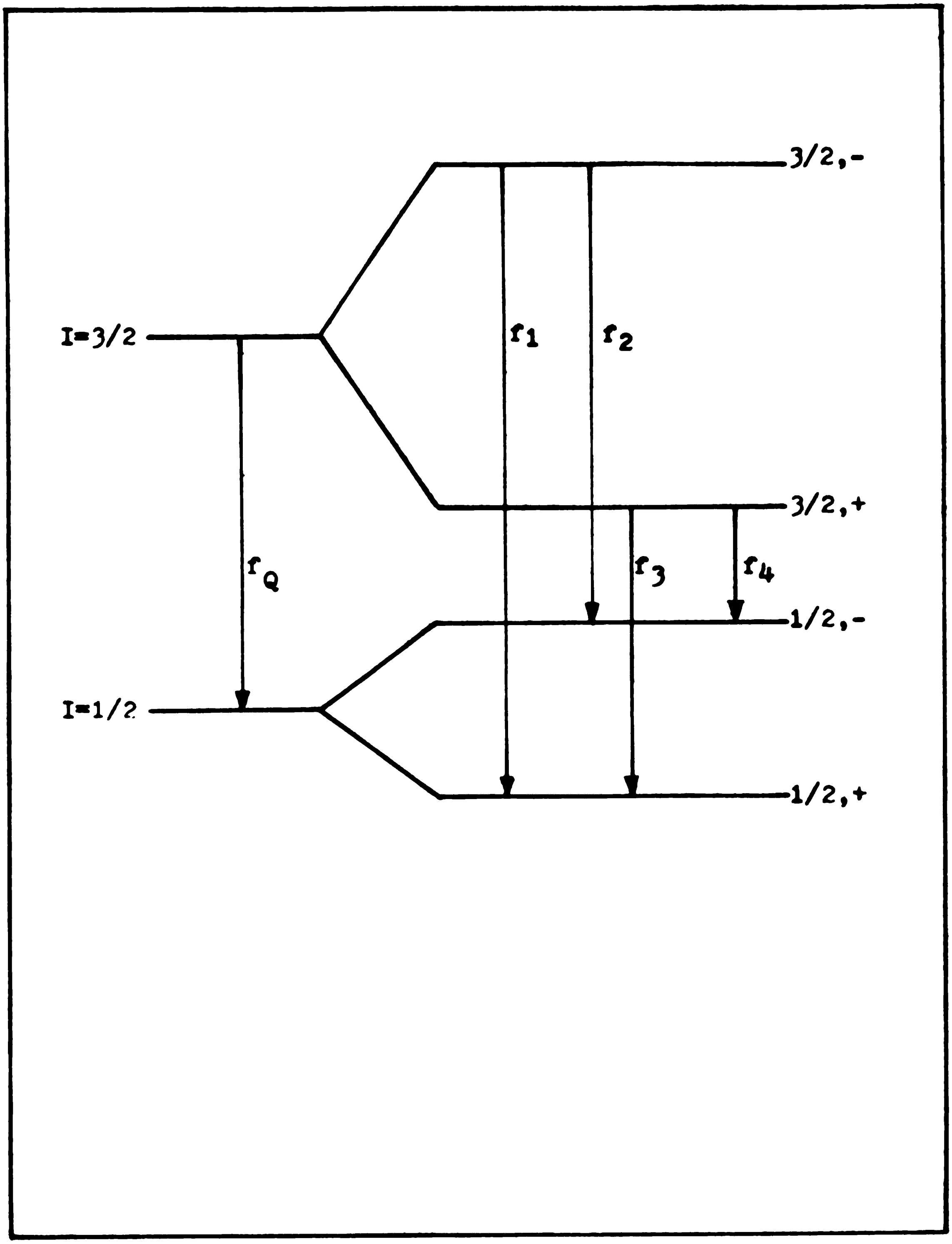

Figure 15: Zeeman splitting of pure quadrupole spectrum

Rewriting the equations for the energy levels in terms of the magnetic field, the frequencies become:

$$f_1 = f_Q + (\gamma\hbar H/2h)\{[3/2] + [1/2]\} \qquad (A55)$$

$$f_2 = f_Q + (\gamma\hbar H/2h)\{[3/2] - [1/2]\} \qquad (A56)$$

$$f_3 = f_Q - (\gamma\hbar H/2h)\{[3/2] - [1/2]\} \qquad (A57)$$

$$f_4 = f_Q - (\gamma\hbar H/2h)\{[3/2] + [1/2]\} \qquad (A58)$$

For η large enough, all four transitions corresponding to the frequencies $f_1 \ldots f_4$ are possible. It should be obvious that for the central pair of lines f_2 and f_3, there are certain orientations of the magnetic field for which $[3/2] = [1/2]$, and $f_2 = f_3$ ($= f_Q$ in the perturbation picture, although this is not true in general). If the frequencies and angles are known for these orientations where $f_2 = f_3$, one may deduce the internal magnetic field of the crystal.

APPENDIX B

COMMENTS ON TEMPERATURE DEPENDENCE

With an applied magnetic field of 1500 G along the line of intersection of the cleavage and xz planes of the crystal, the frequency of a strong line was measured at intervals as the temperature was lowered from 4.2 K to 1.22 K. Data is presented in Table 10; f vs. T is plotted in Figure 16.

The transferred hyperfine effect should have strong temperature dependence due to its dependence on the spin thermal average. The interaction is negligible at 77 K, but quite pronounced at 4.2 K. From Section X, equations (107) and (109), one sees that in the xz plane the transferred hyperfine field opposes the applied field. Hence the decrease in frequency of the line with temperature may be attributed to a cancelling of the applied field by the transferred hyperfine field, and hence a decrease in the magnitude of the Zeeman interaction.

All of the data to which the $\underline{\underline{T}}$ tensor has been fitted was taken at the lowest attainable temperature of the cryostat, and He^4 vapor pressures were periodically monitored with a Baratron. Vapor pressures averaged 540 microns, corresponding to 1.18 K, but varied between 534 and 546 microns, a maximum spread in temperature of 0.003 K.

Referring to Figure 16, the low temperature portion of the curve is almost a straight line. By calculating the slope of the lower portion and using a ΔT of 0.003 K, one predicts a Δf of about 0.4 kHz in the transition frequency. Since this is less than the uncertainty in measuring even a very strong line, temperature fluctuations during the experiments can be discounted as a significant cause of error.

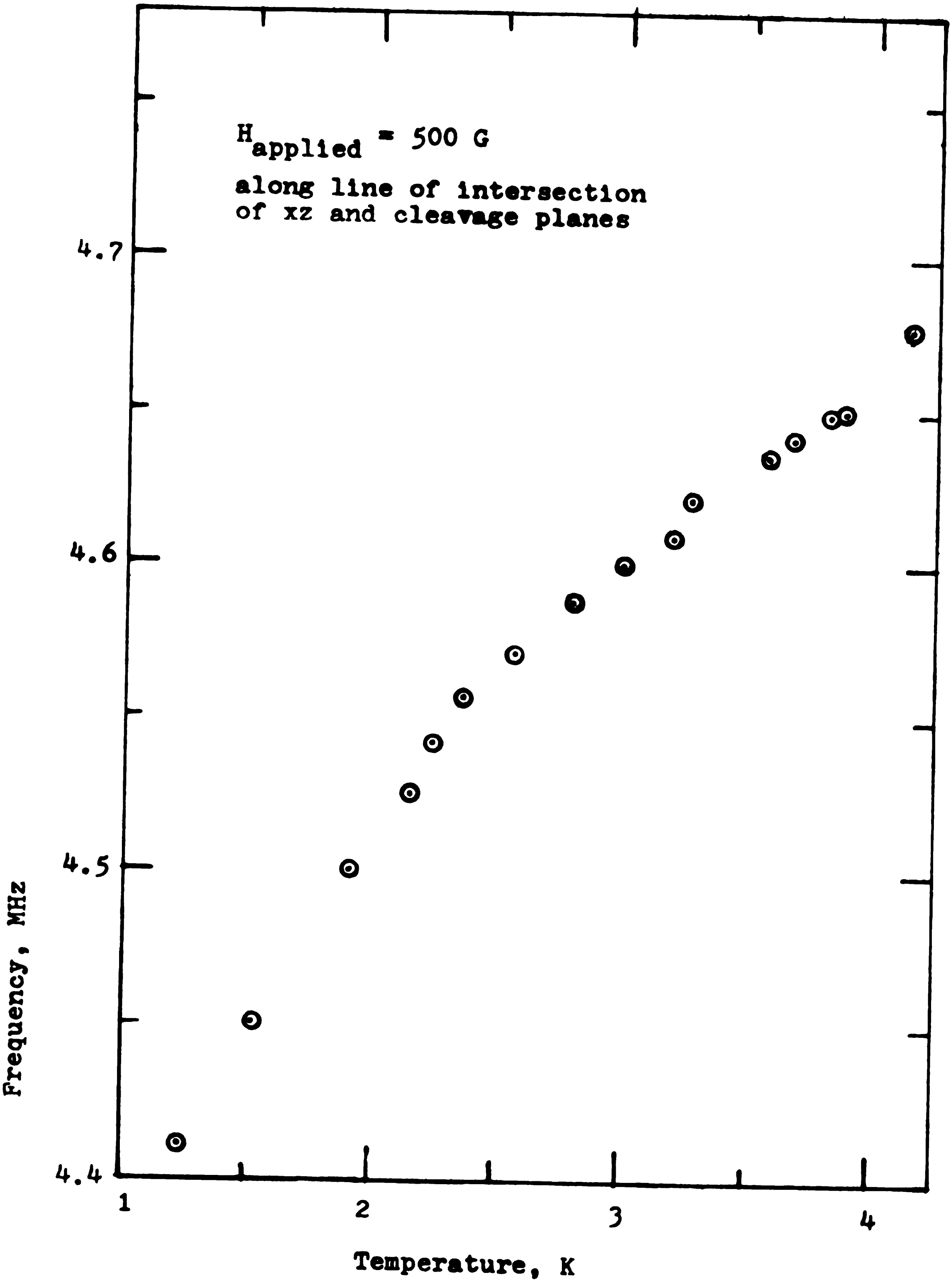

Figure 16: Frequency vs. temperature for a signal

TABLE 10

Variation of Frequency with Temperature

Applied field H = 1500 G along the line of intersection of the cleavage and xz planes, four-fold site. (See Figure 16)

T,K	f, kHz
4.13	4685.4
3.87	4651.0
3.82	4648.5
3.68	4640.9
3.57	4635.9
3.27	4621.9
3.20	4609.0
3.00	4599.6
2.79	4588.5
2.57	4571.1
2.40	4557.6*
2.23	4542.5*
2.15	4525.2
1.93	4504.0
1.53	4451.5
1.22	4411.4

*denotes a structured or blended signal

APPENDIX C

COMMENTS ON THE THREE-FOLD AXIS OF SYMMETRY

In Section VII, which discusses the kind of data taken and presents the results graphically, there is experimental evidence that the effective field tensor $\underline{\underline{T}}$ has the same three-fold symmetry property as the crystal structure. This axis of symmetry is perpendicular to the cleavage plane. It is desirable to explore this three-fold character of the four-fold and eight-fold sites further by using the fitted $\underline{\underline{T}}$ tensor and program EYEBAL to generate the transition frequencies for rotations of the applied field in various planes in the crystal.

It will be recalled that the $\underline{\underline{T}}$ tensor was fitted to the four-fold site data. Hence, in testing for the existence of the three-fold axis using the computer, one must first establish whether the $\underline{\underline{T}}$ tensor is different for the eight-fold site. By symmetry, it was reasoned that the $\underline{\underline{T}}$ tensors for the two sites would be much alike. Hence, $\underline{\underline{T}}$ for the four-fold site was adopted as a starting point, and an attempt was made to fit this tensor to the eight-fold site data.

Many fits were attempted, using the method of Section VIII. An immediate problem was that resolution for the eight-fold sites was not as good as for the four-fold site. Many of the signals were very broad, and repeatability of measurement was poor. Some of the attempted fits corrected the curves of transition frequencies well over certain regions of the spectrum, but always at the expense of a good fit to data taken at other angles.

After many attempts, it was concluded that the $\underline{\underline{T}}$ tensor from the four-fold site data gave the best overall fit to the eight-fold site data. As far as could be determined, the $\underline{\underline{T}}$ tensors measured in the principal axis system were identical for both four-fold and eight-fold sites. However, due to scatter in the eight-fold site data, the error bars on the eight-fold site tensor should be at least a factor of four larger than the error bars on the four-fold site tensor.

It is found that program EYEBAL closely predicts the eight-fold site transition frequencies for all orientations of the crystal. Since the program does this using an Eulerl orientation angle of ±120° as input, the three-fold magnetic character of these sites is corroborated.

APPENDIX D

Data Tables

TABLE 11

Data for the elliptical cone method of locating the principal axes, four-fold site, f_Q = 4515.7 kHz

ϕ_{lab}, °	θ_{lab}, °	ϕ_{lab}, °	θ_{lab}, °
350	298.5	160	9, 189
345	300.2	140	10, 190
335	300.2	120	11, 191
325	297	100	no obs.
315	289	80	no obs.
305	278	0	295
295	264	5	291
285	243	10	286
275	229	15	281
265	38, 218	20	273
255	29, 209	25	264
245	21, 201	30	255
235	17, 197	35	247
225	14, 194	40	238
215	14, 194	45	229
205	12, 192	50	43, 223
195	11, 191	60	31, 211
180	10, 190	70	no obs.

TABLE 12

H in cleavage plane, f_n in kHz

four-fold site, y at 15°

ϕ_{lab}, °	f_1	f_2	f_3	f_4	strengths
105.0	0.0	4556.6	4480.6	0.0	QDDQ
110.0	4622.4	4558.9	4477.1	4414.8	AADF
120.0	0.0	4581.6	4458.5	4395.8	QAAF
130.0	0.0	4608.0	4431.8	0.0	QAAQ
140.0	0.0	4638.0	4404.4	4329.5	QAAF
150.0	4744.2	4665.9	4377.8	0.0	FAAQ
160.0	0.0	4688.3	4356.7	0.0	QAAQ
170.0	0.0	4705.6	4340.3	0.0	QAAQ
0.0	4823.6	4718.2	4328.3	4238.9	FABF
10.0	4813.8	4723.9	4323.5	0.0	FAAQ
20.0	4820.9	4722.9	4324.2	0.0	FAAQ
30.0	4815.3	4716.0	4330.7	4231.8	FACD
40.0	4794.0	4704.6	4340.3	4250.6	DACF
50.0	4769.6	4684.7	4358.0	0.0	FAAQ
60.0	4742.9	4660.2	4378.6	4295.7	DCAF
70.0	4713.4	4633.5	4406.8	4327.6	FAAD
80.0	0.0	4606.8	4432.3	4350.1	QCCA
85.0	0.0	4595.4	4443.5	4376.2	QAEC
90.0	0.0	4578.6	4456.7	4392.1	QDGD
100.0	4621.4	4557.7	4478.8	4417.4	FAAF

Table 12 (cont'd)

eight-fold sites

ϕ_{lab}, °	f_1	f_2	f_3	f_4	strengths
105.0	0.0	4630.6	4291.5	0.0	QAAQ
110.0	0.0	4622.4	4298.1	0.0	QAAQ
120.0	4679.0	4596.6	4324.7	0.0	FAAQ
130.0	0.0	4565.3	4352.7	0.0	QCAQ
140.0	4620.9	4530.3	4382.0	4294.3	FEFQ
150.0	4586.2	4498.0	4415.8	4328.8	AGGD
160.0	4562.4	4471.7	4443.9	0.0	DGFQ
170.0	4560.8	4469.4	4443.1	0.0	DDDQ
180.0	4587.4	4493.4	4421.0	0.0	DEEQ
0.0	4588.8	4494.4	4419.1	0.0	DEEQ
10.0	4621.0	4529.8	4386.5	0.0	AECQ
20.0	4654.2	4562.8	4357.7	4263.5	DFFD
30.0	4700.4	4595.7	4330.7	4231.8	FDCF
40.0	0.0	4623.2	4302.2	4204.8	QGCF
50.0	0.0	4642.3	4282.1	4184.0	QACF
60.0	0.0	4660.2	4268.6	0.0	QCCQ
70.0	0.0	4662.8	4262.0	0.0	QACQ
80.0	0.0	4663.6	4263.3	4151.2	QAAF
85.0	0.0	4659.6	4266.3	0.0	QAAQ
90.0	0.0	4654.4	4269.5	0.0	QAAQ
100.0	4707.0	4641.0	4282.7	0.0	FAAQ
105.0	0.0	4630.6	4291.5	0.0	QAAQ
110.0	0.0	4648.3	4284.6	0.0	QAAQ
120.0	0.0	4653.5	4270.4	0.0	QAAQ
130.0	0.0	4661.9	4264.4	0.0	QAAQ
140.0	0.0	4660.4	4265.3	0.0	QAAQ
150.0	0.0	4658.0	4271.3	0.0	QAAQ
160.0	0.0	4644.1	4283.6	0.0	QBAQ
170.0	0.0	4625.3	4299.5	0.0	QACQ
180.0	0.0	4603.0	4320.7	0.0	QAAQ
10.0	0.0	4574.4	4346.9	0.0	QADQ
20.0	0.0	4548.0	4373.9	0.0	QAAQ
30.0	0.0	4516.6	4401.0	0.0	QAAQ
40.0	4567.0	4496.4	4419.8	0.0	FDDQ
50.0	4571.3	4497.2	4420.3	0.0	FDAQ
60.0	4589.2	4514.0	4403.4	0.0	DDDQ
70.0	0.0	4541.3	4377.6	0.0	QDDQ
80.0	0.0	4569.4	4377.7	0.0	QAAQ
85.0	0.0	4595.4	4336.2	0.0	QDCQ
90.0	0.0	4599.5	4326.6	0.0	QACQ
100.0	0.0	4621.4	4300.7	0.0	QEAQ
0.0	0.0	4603.0	0.0	0.0	QAQQ

TABLE 13

H in xz plane, four-fold site

four-fold site f_n in kHz

θ_{lab}, °	f_1	f_2	f_3	f_4	strengths
270.	0.	4556.6	4480.6	0.	QDDQ
275.	0.	4570.1	4469.4	0.	QAAQ
280.	0.	4579.0	4464.0	0.	QBBQ
285.	0.	4584.3	4462.4	0.	QAAQ
290.	0.	4586.0	4462.0	0.	QAAQ
295.	0.	4587.8	4464.0	0.	QAAQ
300.	0.	4587.1	4465.7	0.	QAAQ
305.	4728.7	4585.3	4468.7	4329.9	GAAD
310.	0.	4584.2	4472.0	4319.9	QAAE
315.	4754.7	4582.3	4476.9	4309.3	FAAD
320.	4761.9	4577.9	4480.4	4320.0	FAAX
325.	4773.7	4574.2	4485.9	4289.2	FAAD
330.	4779.8	4569.2	4491.4	4283.4	DAAD
335.	4782.5	4563.9	4496.9	4277.2	FAAA
340.	4786.7	4558.0	4501.7	4274.2	AAAA
345.	4788.5	4552.7	4507.0	4270.3	DAAA
350.	4787.2	4544.9	4510.7	4270.5	DDAA
355.	4780.1	4519.1	4536.	4272.9	FAXA
0.	4774.7	4524.7	4527.	4273.9	DCXD
0.	4774.7	4524.7	4527.	4273.9	DCXD
5.	4771.7	4527.5	4522.	4277.8	FAXD
10.	4763.9	4532.1	4517.3	4285.3	DXFD
15.	4753.	4538.4	4507.0	4290.9	XAAF
20.0	4744.8	4542.6	4495.9	4299.5	FACD
25.0	4736.9	4547.2	4491.3	4314.3	FAAF
30.0	4717.	4552.5	4486.4	4317.8	XAAE
35.0	4700.2	4555.9	4476.6	4339.4	FAAF
40.	4676.1	4559.1	4472.4	4385.5	FCCF
45.0	4665.5	4564.7	4469.1	4366.3	FCCG
50.0	4637.4	4568.7	4466.6	4387.2	FCAF
55.0	4625.	4567.9	4463.1	0.	XAAQ
60.0	4616.2	4566.0	4465.6	0.	ECAQ
65.0	4610.	4557.2	4474.4	0.	XCCQ
70.0	4605.9	4543.8	4486.5	4427.2	AAAA
75.	4605.1	4525.9	4505.3	4428.8	AAAA
80.0	4606.9	4515.2	4515.2	4425.8	ACCA
85.	0.	4541.0	4494.1	4420.0	QDDD

Table 13 (cont'd)

eight-fold site

θ_{lab}, °	f_1	f_2	f_3	f_4	strengths
0.0	4736.3	4476.1	0.0	4198.8	CAQA
5.00	4739.1	4472.2	4460.6	4201.3	FCCA
10.	4738.6	4465.6	4465.6	4198.0	ABBA
15.0	4742.0	4478.2	4457.3	4194.6	XFAD
20.0	4744.8	4495.9	4441.8	4190.8	FCFD
25.0	4748.1	0.0	4429.5	4182.7	FQDD
30.0	4751.2	0.0	4422.1	4181.8	DQEE
35.0	4754.7	0.0	4404.8	4183.8	FQFF
40.	4754.9	0.0	4389.1	4182.8	FQEE
45.0	4751.0	0.0	4366.3	4183.3	FQGF
50.0	4745.7	0.0	0.0	4183.2	EQQE
55.0	0.0	0.0	4340.1	0.0	QQFQ
60.0	4737.6	4616.2	4322.6	4194.1	FEEG
65.0	4731.4	4622.5	4313.0	4193.0	FCXX
70.0	4733.9	4626.9	4300.7	4193.0	FACE
75.0	4730.9	4635.7	4292.5	4196.7	FCCF
80.0	4727.1	4640.0	4288.2	4195.0	FXCX
85.0	0.0	4635.1	4288.2	0.0	QAAQ
270.	0.0	4630.6	4291.5	0.0	QAAQ
275.	0.0	4624.0	4293.7	0.0	QACQ
280.	4733.3	4619.5	4305.1	4191.8	DBEE
285.	4734.8	4606.5	4326.9	4189.5	FFFE
290.	4738.7	4586.	4333.0	4180.0	FCED
295.	4734.6	0.0	4341.4	4180.1	FQFF
300.	4738.0	4550.	4359.5	4179.9	GXDF
305.	4728.7	4526.9	4373.4	0.0	XDDQ
310.	4728.6	4512.2	4395.6	4192.7	EDGG
315.	4733.4	4495.0	4410.0	4196.0	FXXX
320.	4723.6	4480.4	4422.8	4202.3	FADG
325.	4720.8	4464.0	4428.3	4202.4	FXFD
330.	4718.9	4448.7	4448.7	4202.9	DEEF
335.	4719.7	4476.0	4449.3	4208.3	FAAA
340.	4719.7	0.0	4445.4	4208.5	DQDE
345.	4720.1	4474.1	4440.4	4200.	DAAE
350.	4733.3	4477.	4440.5	4204.7	EXDC
355.	4734.5	4476.2	4439.8	4202.7	AAFF

TABLE 14

H in plane ⊥ cleavage, containing y of four-fold site

four-fold site f_n in kHz

θ_{lab}, °	f_1	f_2	f_3	f_4	strengths
0.0	4779.5	4524.5	4524.5	4274.1	ACCF
10.0	4781.0	4525.1	4525.1	4274.9	FCCD
15.0	4778.6	4531.7	4517.1	0.0	FDAQ
20.0	4785.2	4545.7	4509.6	4267.2	FAAA
25.0	4790.2	4555.6	4495.9	4260.0	DDEF
30.0	4799.3	4568.3	4488.0	4255.8	DAED
35.0	4801.2	4582.2	4468.2	4248.6	DDDD
40.0	4808.8	4597.4	4449.4	4241.1	ADDA
45.0	4814.7	4613.9	4437.2	4239.2	DDDF
50.0	4816.5	4629.4	4408.3	4234.7	DACA
60.0	4823.4	4664.3	0.0	4229.6	DCQA
70.0	4821.8	4690.1	0.0	4227.4	DAQD
80.0	4822.7	4713.7	4333.8	4226.4	DAAD
270.0	0.0	4725.0	4323.3	0.0	QAAQ
290.0	4823.4	4708.9	4338.1	4227.0	FDAA
300.0	4821.8	4692.0	4361.1	4225.3	DAAA
310.0	4822.7	4660.8	4392.8	4229.1	DACD
315.0	4822.2	4641.3	4407.4	4233.0	DFED
320.0	4812.0	4631.1	0.0	4233.7	DDQE
325.0	4815.0	4611.6	0.0	0.0	GFQQ
330.0	4806.6	4596.8	0.0	4246.0	FFQD
335.0	4804.6	4578.9	0.0	0.0	FFQQ
340.0	4794.0	4559.9	0000.0	4257.5	FFQF
345.0	4783.0	4551.6	4506.7	0.0	XDDQ
350.0	4783.7	4541.4	4514.8	4266.5	FDFF

Table 14 (cont'd)

eight-fold sites

θ_{lab}, °	f_1	f_2	f_3	f_4	strengths
0.0	4734.3	4477.3	4460.0	4199.5	DACA
10.0	4733.8	4484.5	4449.5	4200.4	AADA
15.0	4735.3	4486.1	4442.6	4202.1	DDDE
20.0	0.0	4488.0	4440.4	4202.8	QXFA
25.0	4712.9	4495.9	0.0	4210.9	FEQD
30.0	4705.5	4488.0	4445.9	4211.8	FEDD
35.0	4704.1	0.0	0.0	0.0	FQQQ
40.0	4692.6	4475.0	4449.4	4220.6	FXEF
45.0	4689.7	4465.5	4461.4	0.0	DGGQ
50.0	4676.4	4458.7	4458.7	4234.7	FCCC
60.0	4664.3	4471.7	4440.8	4247.5	CFAX
70.0	4656.4	4498.4	4416.5	4258.7	FDDF
80.0	4644.0	4525.1	4391.5	4267.7	DDDF
270.0	4637.0	4561.2	4367.8	4281.7	DAAA
280.0	4640.0	4561.4	4361.0	4279.4	AAAE
290.0	4645.3	4564.7	4361.7	4271.8	DAAA
300.0	4661.1	4555.3	4376.2	4255.2	FAAF
310.0	4687.0	4539.9	4392.8	4243.0	XACX
315.0	0.0	4533.7	4407.4	0.0	QDEQ
320.0	4712.7	4523.8	4413.0	4233.7	AFAE
325.0	4721.6	4515.7	4426.1	4223.8	FDDE
330.0	4729.6	4507.9	4435.7	4214.0	FAAD
335.0	4737.2	4494.8	4445.8	4207.3	FDDE
340.0	4737.4	4494.1	4449.8	4206.1	FDAF
345.0	4736.8	4480.9	4457.0	4205.5	DDAD
350.0	4738.1	4472.4	4464.0	4200.9	DAAA
270.0	0.0	0.0	4359.8	0.0	QQAQ
280.0	0.0	0.0	4370.7	0.0	QQFQ
290.0	0.0	4516.7	4396.4	0.0	QDAQ
300.0	0.0	4492.5	4422.1	0.0	QDAQ
310.0	0.0	0.0	4443.5	0.0	QQFQ
315.0	0.0	4460.6	0.0	0.0	QFQQ
320.0	0.0	4459.2	4452.6	0.0	QDAQ
15.0	0.0	4469.7	4469.7	0.0	QAAQ
25.0	0.0	4483.0	4456.7	0.0	QEEQ
30.0	0.0	4488.0	0.0	0.0	QEQQ
35.0	0.0	4501.7	4438.6	0.0	QDAQ
40.0	0.0	4511.3	4429.2	0.0	QAAQ
45.0	0.0	4519.7	4420.3	0.0	QFAQ
50.0	0.0	4528.3	4408.3	0.0	QACQ
60.0	0.0	4543.7	4390.4	0.0	QAAQ
70.0	0.0	4557.9	4372.3	0.0	QADQ
80.0	0.0	4565.9	4359.7	0.0	QAAQ

TABLE 15

H in xz plane of eight-fold site

eight-fold site, f_n in kHz

θ_{lab}, °	f_1	f_2	f_3	f_4	strengths
270.	4559.7	4489.8	4424.4	4363.6	ADFA
275.	4559.7	0.	4439.0	0.	AXDX
280.	4553.8	4454.7	4454.7	4364.9	DAAA
285.	4553.4	4472.9	4438.9	0.	DFDX
290.	0.	4485.0	4421.5	4373.0	XFFA
295.	0.	4506.0	4409.3	0.	XADX
300.	0.	4514.7	4397.6	0.	XAFX
305	4575.2	0.	0.	4350.0	EXXD
310.	0.	4516.7	4395.1	0	XAAX
320.	0.	4513.9	4403.1	0.	XAAX
330.	0.	4409.6	4411.2	0.	XAAX
350.	0.	4495.5	4435.0	0.	XEFX
0.	0.	4479.3	4453.7	4203.9	XCFD
10.	0.	0.	4468.1	4201.9	XXAA
20.	4730.7	4482.2	4457.6	4208.5	EAFD
30.	0.	4495.6	4440.6	0.	XACX
40.	0.	4505.8	4428.8	0.	XAAX
50.	0.	4511.3	4417.7	0.	XAAX
60.	0.	4515.3	4414.6	0.	XAAX
70.	0.	4519.3	4408.4	0.	XAAX
80.	0.	4508.5	4412.4	0.	XACX

Table 15 (cont'd)

four-fold site

θ_{lab}, °	f_1	f_2	f_3	f_4	strengths
270.	0.	4681.8	4365.5	0.	XAAX
275.	0.	0.	4359.4	0.	XXAX
280.	0.	4680.1	4364.9	0.	XAAX
285.	0.	0.	4366.9	0.	XXAX
290.	0.	4671.0	4380.4	0.	XADX
300.	0.	4656.6	0.	0.	XAXX
310.	0.	4631.4	4428.5	0.	XACX
320.	0.	4607.8	4451.5	0.	XAEX
330.	0.	4584.6	4471.6	0.	XAEX
340.	0.	4562.2	0.	0.	XAXX
350.	4789.0	4542.9	0.	4266.2	ACXD
0.	4779.2	4525.1	0.	4275.2	AAXA
10.	4769.4	4528.1	0.	4279.0	AAXA
20.	4751.4	4519.4	0.	4283.9	AAXA
40.	0.	4563.2	0.	0.	XDXX
50.	0.	4585.9	4455.3	0.	XAFX
60.	0.	4616.6	0.	0.	XAXX
70.	0.	4641.9	0.	0.	XDXX
80.	0.	4663.5	4379.6	0.	XCAX
90.	0.	4680.4	4363.6	0.	XAAX